remote sensing

MDPI

Article

Performance Evaluation and Spatiotemporal Dynamics of Nine Reanalysis and Remote Sensing Evapotranspiration Products in China

Yujie Liu, Wen Wang *, Tianqing Zhao and Zhiyuan Huo

The National Key Laboratory of Water Disaster Prevention, Hohai University, Nanjing 210098, China
* Correspondence: wangwen@hhu.edu.cn

Abstract: Evapotranspiration (ET) is a critical component of the hydrological cycle. The eddy covariance data at 40 flux stations in different climatic regions in China were used to evaluate the accuracy of five reanalysis actual ET datasets (ERA5, ERA5-LAND, GLDAS-2.1, MERRA-2, TerraClimate) and four remote sensing estimation ET datasets (ETMonitor, GLEAM4.2a, PML_V2, SiTHv2), which are widely used by the hydrometeorological and climatological communities, in terms of the root mean square error, Pearson correlation coefficient, mean absolute deviation, and Taylor skill score. The results show that remote sensing products outperform reanalysis datasets. Among them, ETMonitor has the highest accuracy, followed by PML_V2 and SiTHv2. TerraClimate and MERRA-2 have the least agreement with the observations at flux sites across nearly all evaluation metrics. All products can capture the seasonality of ET in China, but underestimate ET in northwest China and overestimate ET in southern China throughout the year. We tried to merge three optimal data products (ETMonitor, PML_V2, and SiTHv2) using the triple collocation analysis method to improve the ET estimation, but the results showed that the improvement by the data fusion approach is marginal. The estimation of the multi-year average evapotranspiration during the period from 2001 to 2020 ranges from 397.8 mm/year (GLEAM4.2a) to 504.8 mm/year (ERA5-Land) in China. From 2001 to 2020, annual evapotranspiration in China generally increased, but with varying rates across different products. MERRA-2 showed the largest annual increase rate (3.71 mm/year), while SiTHv2 had the smallest (0.17 mm/year). There are no significant changes in the seasonality of ET by most ET products from 2001 to 2020, except for PML_V2 and SiTHv2, which indicate an increase in seasonality in terms of the evapotranspiration concentration index. This ET intercomparison addresses a key knowledge gap in terrestrial water flux quantification, aiding climate and hydrological research.

Keywords: actual evapotranspiration; remote sensing; reanalysis data; ET evaluation; triple collocation analysis

check for updates

Academic Editor: Guido D'Urso

Received: 12 March 2025
Revised: 21 May 2025
Accepted: 26 May 2025
Published: 28 May 2025

Citation: Liu, Y.; Wang, W.; Zhao, T.; Huo, Z. Performance Evaluation and Spatiotemporal Dynamics of Nine Reanalysis and Remote Sensing Evapotranspiration Products in China. *Remote Sens.* **2025**, *17*, 1881. https://doi.org/10.3390/rs17111881

Copyright: © 2025 by the authors. Licensee MDPI, Basel, Switzerland. This article is an open access article distributed under the terms and conditions of the Creative Commons Attribution (CC BY) license (https://creativecommons.org/licenses/by/4.0/).

1. Introduction

Evapotranspiration (ET) is an important part of the Earth's water cycle, and its accurate estimation is of great significance for water resource allocation, irrigation management, climate model calibration, and climate change assessment [1,2]. The evapotranspiration process is affected by many environmental factors, such as temperature, humidity, wind speed, precipitation, soil, and vegetation characteristics, and its dynamics in space and time are extremely complex [3]. Remote sensing-based evapotranspiration data and reanalysis data have become important sources to obtain large-scale and long-term evapotranspiration

information for assessing climate change (e.g., [4]). However, as evapotranspiration is influenced by a variety of environmental factors, its estimation typically relies on multiple approaches, each with inherent strengths and limitations. Different models and data sources may yield divergent ET estimates, resulting in substantial uncertainty [5]. Therefore, evaluating the accuracy of various ET products is essential to ensure the reliability of ET estimates.

The remote sensing evapotranspiration data is based on the satellite platform to obtain surface information, such as surface temperature, vegetation index, soil moisture, etc., and then retrieved by the estimation model. The commonly used remote sensing evapotranspiration estimation methods include models combined with traditional methods (such as the Penmen–Monteith model, Priestley–Taylor model, etc.), energy balance methods (such as the SEBAL model, Shuttleworth–Wallace dual-source model, etc.), feature space methods, and empirical model methods [6,7]. The main advantages of remote sensing products are their high spatial resolution and wide spatial coverage, which can meet the research needs of large-scale and long-term series. Common remote sensing evapotranspiration products include GLEAM (Global Land Evaporation Amsterdam Model) [8], PML_V2 [9], ETMonitor [10], etc. These products can provide large-scale evapotranspiration information by combining remote sensing images with meteorological data. However, due to the limitations of observation accuracy, data fusion, and model algorithms, the evapotranspiration estimation results of remote sensing inversion still have some errors [11].

Reanalysis data are a kind of high spatiotemporal resolution meteorological field data generated by systematic reconstruction and calibration of historical meteorological observation data based on numerical meteorological models. Common reanalysis products, such as ERA5 (European Meteorological Centre) [12], Global Land Data Assimilation System (GLDAS) [13], and MERRA (NASA Modern Meteorological Reanalysis) [14], provide key information on temperature, precipitation, radiation, and wind speed, and are widely used to drive hydrological models or in conjunction with remote sensing data to estimate evapotranspiration. The strength of the reanalysis data lies in their global consistency, the continuity of longer time series, and their applicability to long-term trend analysis and climate change research.

Both remote sensing data and reanalysis data exhibit large precision uncertainties due to differences in data sources and estimation methods [15–17]. The accuracy of remote sensing data may be affected by surface type, meteorological conditions, and the hypothesis of the inversion model, whereas the reanalysis data may be affected by the errors of the parameterization of the meteorological model and the data assimilation process [18,19]. The accuracy assessment and comparison of different evapotranspiration products are of great theoretical and application value for understanding the advantages and disadvantages of various data products, identifying the sources of errors, and optimizing the evapotranspiration estimation methods. Elnashar et al. [20] evaluated 12 global ET datasets and demonstrated that most of the products showed strong agreement with flux tower observations. Liu et al. [21] evaluated 10 ET products using monthly eddy covariance observations at 206 flux sites on a global scale and found that all products showed comparable performance and that no single product showed the best performance. Shi et al. [22] compared the performance of six ET products in mainland China during 2001–2018 and found that all six products generally showed good agreement with the nine flux sites. Zuo et al. [23] assessed the accuracy of six ET products from 2005 to 2020 across China, and the results revealed that all products effectively captured the ET variations across China, but with significant variability in metrics among these products.

China has a vast territory, diverse climate, and complex terrain, and the characteristics of evapotranspiration in different regions vary greatly. Although several studies have

evaluated the accuracy of ET products in China [17,22–25], they often rely on a limited number of observation sites, and some ET datasets are continuously updated (e.g., recent release of GLEAM 4.2), leading to possible biases in their evaluation results. This study aims to evaluate the accuracy of several widely used evapotranspiration datasets in China, with the goal of providing comprehensive guidance for choosing the most suitable dataset for specific regions. The regional divisions are based on China's four major geographic zones, and the optimal dataset for each region is identified through a synthesis of multiple evaluation metrics. Based on four data quality assessment metrics (root mean square error, Pearson correlation coefficient, mean absolute deviation, and Taylor skill score), we compared the performance of five reanalysis ET datasets (ERA5, ERA5-Land, GLDAS-2.1, MERRA-2, TerraClimate) and four remote sensing-based ET estimation datasets (ETMonitor, GLEAM4.2a, PML_V2, SiTHv2) over China from 2001 to 2020. Given their extensive use and the diversity of their methodological frameworks, evaluating the accuracy of these ET products is essential to ensure the reliability of evapotranspiration estimates [15,20,24,26]. The evaluation was conducted at a monthly scale, utilizing eddy covariance observations from 40 flux tower sites. We expect that the extensive coverage of flux observations would improve the reliability and representativeness of the evaluation outcomes. In Section 2, the collection and processing of ET products and observation data, and the methodology will be introduced; Section 3 presents the results of the overall evaluation, sub-surface type evaluation, sub-region evaluation, and seasonal, spatial, and changing trend analysis. Section 4 discussed the comparison with other evaluation results and the advantages and disadvantages of remote sensing data and reanalysis data. Finally, in Section 5, the conclusions were drawn.

2. Materials and Methods

2.1. The Actual Evapotranspiration Products

Five reanalysis actual evapotranspiration (ET) datasets (ERA5, ERA5-Land, GLDAS-2.1, MERRA-2, TerraClimate) and four remote sensing actual evapotranspiration datasets (ETMonitor, GLEAM4.2a, PML_V2, SiTHv2) in China are evaluated in this study, details can be found in Table 1. Due to their widespread application and the heterogeneity in their underlying methodologies, it is crucial to assess the accuracy of these ET datasets in order to ensure the reliability of evapotranspiration estimates.

Table 1. ET products' information involved in this study.

Product Type	Product Name	Time Resolution	Spatial Resolution	Time Range	Reference
Reanalysis data	ERA5	Monthly	0.25° × 0.25°	1940–2024	Hersbach et al. [27]
	ERA5-Land	Monthly	0.1° × 0.1°	1950–2024	Muñoz Sabater [28]
	GLDAS-2.1	Monthly	0.25° × 0.25°	2000–2024	Beaudoing et al. [29]
	MERRA-2	Monthly	0.5° × 0.625°	1980–2024	GMAO [30]
	TerraClimate	Monthly	0.05° × 0.05°	1958–2024	Abatzoglou et al. [31]
Remote sensing data	ETMonitor	Daily	1 km	2000–2021	Zheng et al. [10]
	GLEAM4.2a	Monthly	0.1° × 0.1°	1980–2023	Miralles et al. [32]
	PML_V2	8-day	500 m	26 February 2000–2020	Zhang et al. [9]
	SiTHv2	Monthly	0.1° × 0.1°	1982–2020	Zhang et al. [33]

2.1.1. Reanalysis Actual Evapotranspiration Datasets

- ERA5

ERA5 is the fifth-generation reanalysis product of the European Centre for Medium-Range Weather Forecasts (ECMWF) on global climate and weather over the past 80 years. The data have been available since 1940, covering the whole world and containing a variety

of meteorological elements. The ERA5 downloaded here has a time resolution of one month and a spatial resolution of 0.25° × 0.25°, which can be obtained from the website (https://cds.climate.copernicus.eu/datasets/reanalysis-era5-single-levels-monthly-means?tab=download) (accessed on 31 January 2025).

- ERA5-Land

ERA5-Land is generated by reprocessing the land part of the ECMWF ERA5 climate reanalysis data. Compared with ERA5, ERA5-Land provides a consistent view of the evolution of land variables over decades with higher resolution. The data have been available since 1950, covering the whole world and containing a variety of variables. The ERA5-Land downloaded here has a time resolution of one month and a spatial resolution of 0.1° × 0.1° and is available from the website (https://cds.climate.copernicus.eu/datasets/reanalysis-era5-land-monthly-means?tab=download) (accessed on 31 January 2025).

- GLDAS-2.1

The construction of the GLDAS (Global Land Data Assimilation System) dataset is based on multi-source satellite observation data and ground observation data. These data are integrated through advanced assimilation techniques to generate global land surface state variables. The dataset covers a variety of meteorological and hydrological variables, such as soil moisture, surface temperature, precipitation, etc. The construction process strictly follows the physical model and data assimilation algorithm to ensure the high accuracy and consistency of the data. Different from GLDAS-2.0, which has been available from 1948 to 2014, GLDAS-2.1 has been available since 2000. The GLDAS-2.1 downloaded here has a time resolution of one month and a spatial resolution of 0.25° × 0.25° and is available from the website (https://disc.gsfc.nasa.gov/datasets?keywords=GLDAS) (accessed on 31 January 2025).

- MERRA-2

MERRA-2 (Modern-Era Retrospective analysis for Research and Applications, Version 2) is a global meteorological reanalysis dataset provided by the National Aeronautics and Space Administration (NASA), which aims to provide high spatial and temporal resolution data of global meteorological and hydrological variables from 1980 to the present. The data cover multiple meteorological elements, such as temperature, precipitation, radiation, wind speed, and humidity, and are widely used in climate research, weather forecasting, and hydrological simulation. The MERRA-2 downloaded here has a time resolution of one month and a spatial resolution of 0.5° × 0.625°, which can be obtained from the website (https://disc.gsfc.nasa.gov/datasets?project=MERRA-2) (accessed on 31 January 2025).

- TerraClimate

TerraClimate is a global monthly climate and water balance dataset covering climate data from 1958 to the present. The dataset includes variables such as temperature, precipitation, evapotranspiration, runoff, snow water equivalent, potential evapotranspiration, and soil moisture. The dataset achieves the accurate estimation of global climate variables by integrating data from various satellite sensors and using advanced climate models and data assimilation techniques. TerraClimate downloaded here has a temporal resolution of months and a spatial resolution of 0.05° × 0.05° and is available from the website (https://www.climatologylab.org/terraclimate.html) (accessed on 31 January 2024).

2.1.2. Remote Sensing Actual Evapotranspiration Datasets

- ETMonitor

ETMonitor data are generated by combining the ETMonitor model with multi-source remote sensing data and reanalysis data. The ETMonitor remote sensing evapotranspiration

model is based on the mechanism of energy and water exchange on the land surface, such as energy balance, water balance, and plant physiological processes. Parameterization schemes are established for evapotranspiration components to estimate the pixel-scale evapotranspiration components and accumulate the actual evapotranspiration of the pixel land surface. Data are available for the whole world from 2000 to 2021. The ETMonitor downloaded here has a temporal resolution of day and a spatial resolution of 1 km, which can be obtained from the following website (https://data.casearth.cn/dataset/640f012a819aec3f2b52a4b6) (accessed on 31 January 2025).

- GLEAM4.2a

The GLEAM data are a global-scale evapotranspiration estimation product that provides data on different components of evapotranspiration: transpiration, bare soil evaporation, interception loss, evaporation and sublimation in open waters, and other related variables, such as surface and root zone soil moisture, sensible heat flux, potential evaporation, and evaporation stress conditions. This study uses the latest version of GLEAM4.2a, based on satellite and reanalysis data, which has higher spatial resolution (0.1°) and longer timing than the previous version. The time resolution of GLEAM4.2a downloaded here is monthly, and the spatial resolution is $0.1^\circ \times 0.1^\circ$, which can be obtained from the website (https://www.gleam.eu/) (accessed on 31 January 2025).

- PML_V2

The global PML _ V2 land evapotranspiration and total primary productivity dataset is based on the Penman–Monteith–Leuning (PML) model. According to the stomatal conductance theory, the GPP process is coupled, including total primary productivity, vegetation transpiration, soil evaporation, canopy interception evaporation, and water, ice, and snow evaporation, a total of five elements. The PML_V2 data downloaded here have a temporal resolution of 8 days and a spatial resolution of 500 m. Evapotranspiration is the sum of three elements: vegetation transpiration, soil evaporation, and canopy interception evaporation. Data can be obtained from Google Earth Engine (https://developers.google.com/earth-engine/datasets/catalog/CAS_IGSNRR_PML_V2_v017?hl=en) (accessed on 31 January 2025).

- SiTHv2

SiTHv2 is a new global ET and soil moisture dataset with long-term coverage and high spatial and temporal resolution. It is based on a newly developed simple terrestrial hydrosphere model, driven by hydrometeorological variables from multi-source satellite observations and reanalysis data, and takes into account the combined effects of root vertical distribution, multi-layer soil moisture content, and groundwater level changes. The SiTHv2 downloaded here has a time resolution of one month and a spatial resolution of $0.1^\circ \times 0.1^\circ$, which can be obtained from the website (https://data.tpdc.ac.cn/en/data/bc51e1b0-494c-4cd5-ae4d-eba6b9d2322c) (accessed on 31 January 2025).

2.2. Observation Data

China Flux Observation and Research Network (ChinaFLUX) is a long-term monitoring platform covering major ecosystem types and climatic zones across China. It provides standardized measurements of carbon, water, and energy fluxes using eddy covariance techniques [34]. In this study, flux tower data were obtained from the ChinaFLUX network, which is subjected to rigorous quality control procedures, including the removal of outliers and instrument errors, uncertainty classification of flux measurements, gap-filling using methods such as MDS, and data standardization. The datasets are accessible via the official ChinaFLUX website: http://www.chinaflux.org/ (accessed on 31 January 2025).

The latent heat data are retrieved from 40 flux observation stations published by ChinaFLUX. These sites are distributed in four different geographical areas in China, including the northern temperate monsoon climate zone (14 carbon and water flux stations), the northwestern temperate continental climate (7), the alpine climate zone of the Tibet Plateau (7), the southern subtropical monsoon climate zone (12), and six types of underlying surface types, including cropland (8), desert (1), forest (13), grassland (10), shrubland (4), and wetland (4). The specific distribution location is shown in Figure 1. A more detailed description of the 40 flux observation stations (including land cover, data length, etc.) can be found in Appendix A Table A1.

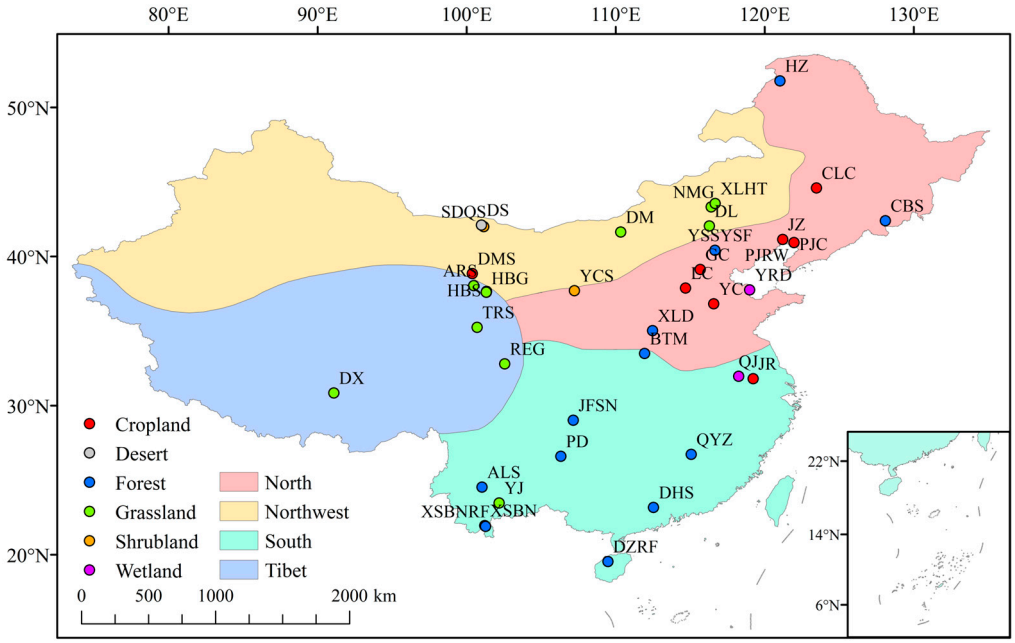


Figure 1. Spatial distribution of regions and observation stations.

Since most of the time resolution of the product data used are monthly, most of the observation data are 30 min latent heat data (W/m^2). The flux observation data are converted to the monthly value of ET by the following [35]:

$$ET_{month} = \sum_{i=1}^{48N} \frac{LE_i \times 60 \times 30}{(2.501 - 0.002361 \times T_i) \times 10^6} \quad (1)$$

where ET_{month} is the monthly cumulative ET (mm); ET_i is the actual evapotranspiration per 30 min (mm); LE_i is the latent heat flux per 30 min (W/m^2); T_i is the temperature (°C); N indicates the number of days in a month.

2.3. Metrics for Accuracy Evaluation

ET products are evaluated at the monthly time scale and the 0.1° × 0.1° spatial resolution. For products not originally available at the monthly scale (e.g., daily-scale ETMonitor and 8-day-scale PML_V2), temporal aggregation is performed to convert them to monthly values. ET datasets with spatial resolutions other than 0.1° × 0.1° are resampled using bilinear interpolation.

The root mean square error (RMSE), Pearson correlation coefficient (r), mean absolute deviation (MBE), and Taylor skill score (TS) are used to comprehensively measure the

overall performance of ET products relative to flux observation data. These metrics are expressed as follows [20]:

$$RMSE = \sqrt{\frac{1}{N}\sum_{i=1}^{N}(X_i - Y_i)^2} \quad (2)$$

$$r = \frac{\sum_{i=1}^{N}(X_i - \overline{X})(Y_i - \overline{Y})}{\sqrt{\sum_{i=1}^{N}(X_i - \overline{X})^2 \sum_{i=1}^{N}(Y_i - \overline{Y})^2}} \quad (3)$$

$$MBE = \frac{1}{N}\sum_{i=1}^{N}(X_i - Y_i) \quad (4)$$

$$TS = \frac{4(1+r)}{\left(\hat{\sigma} + \frac{1}{\hat{\sigma}}\right)^2 (1 + r_0)} \quad (5)$$

where N represents the number of samples; X and Y represent product ET and site ET, respectively; $\overline{X}$ and $\overline{Y}$ represent the mean values of product ET and site ET, respectively; the subscript i represents the ith sample. r_0 is the theoretical maximum r (equal to 1 in this study); $\hat{\sigma}$ indicates the standard deviation of the ET product value divided by the standard deviation of the site value. In general, the higher TS and r, the closer MBE and RMSE are to zero, the better ET products perform.

The Taylor Diagram is a graphical tool used to evaluate the consistency between product data and observation data. It comprehensively displays standard deviation (SD), r, and RMSE through the polar diagram, so that researchers can intuitively compare the differences between multiple product data and observation data. The radial distance represents the standard deviation ratio, and the angle represents the r. The smaller the angle is, the stronger the correlation is. The observed mark in the figure is the location of the observation result. The closer the product data result is to this point, the more consistent the product data are with the observation data, and the higher the evaluation accuracy is. Taylor Diagram concisely presents multiple statistics at the same time, which is helpful for model verification and comparison, quickly identifying the advantages and disadvantages of the model, and providing a basis for model selection and optimization.

2.4. Data Fusion Method

Triple Collocation Analysis (TCA) is used to fuse product data to analyze the possibility of improving the accuracy of data products. The TCA method is based on the assumption that there are three independent data sources with different error characteristics, and the error characteristics of these data sources are independent of each other when estimating the same physical quantity. Therefore, TCA can use the error coordination between these independent data sources to estimate the true value of the target physical quantity by combining the information of each data source, and, at the same time, correct the error of each data source [36].

Specifically, TCA uses three data sources X_1, X_2, and X_3 to estimate the same target variable, assuming that the estimated value of each data source can be expressed as follows [37]:

$$X_i = Y + \varepsilon_i \quad (6)$$

where Y represents the true value of the target variable; ε_i is the error, and each error is assumed to be independent and have zero mean.

Then,

$$\begin{cases} X_1 = a_1 Y + \varepsilon_1 \\ X_2 = a_2 Y + \varepsilon_2 \\ X_3 = a_3 Y + \varepsilon_3 \end{cases} \tag{7}$$

By estimating the error covariance matrix R_ε, the covariance matrix between data sources can be further derived so as to optimize the weighted combination of each data source. The form of the covariance matrix is as follows:

$$R_\varepsilon = \begin{bmatrix} Var(\varepsilon_1) & Cov(\varepsilon_1, \varepsilon_2) & Cov(\varepsilon_1, \varepsilon_3) \\ Cov(\varepsilon_2, \varepsilon_1) & Var(\varepsilon_2) & Cov(\varepsilon_2, \varepsilon_3) \\ Cov(\varepsilon_3, \varepsilon_1) & Cov(\varepsilon_3, \varepsilon_2) & Var(\varepsilon_3) \end{bmatrix} \tag{8}$$

The goal of TCA is to obtain the best estimate of the real target variable Y by solving the above equation to minimize the total variance of the error. The optimal estimation formula can be expressed as the weighted average:

$$\hat{Y} = W^T X \tag{9}$$

where W is the weight vector calculated based on the error covariance matrix R_ε. The solution for the weight W is determined by minimizing the inverse matrix of the error covariance.

2.5. Mann–Kendall Trend Test

The Mann–Kendall (M-K) test is a non-parametric trend test that does not depend on the distribution and is usually used to detect whether there is a linear or non-linear trend in time series data [38]. M-K test is insensitive to outliers; even if there are a small number of outliers in the data, it will not have a significant impact on the test results.

$$S = \sum_{i=1}^{n-1} \sum_{j=i+1}^{n} sgn(x_j - x_i) \tag{10}$$

$$sgn(x_j - x_i) = \begin{cases} +1, \ if \ x_j - x_i > 0 \\ 0, \ if \ x_j - x_i = 0 \\ -1, \ if \ x_j - x_i < 0 \end{cases} \tag{11}$$

$$Var(S) = \frac{n(n-1)(2n+5)}{18} \tag{12}$$

$$Z = \begin{cases} \frac{S-1}{\sqrt{Var(S)}} (S > 0) \\ 0 \ (S = 0) \\ \frac{S+1}{\sqrt{Var(S)}} (S < 0) \end{cases} \tag{13}$$

where n is the number of samples, x_i and x_j are the data values of i and j in the time series respectively, sgn(x) is the symbolic function, and Var(S) represents the variance of the statistical variable S. Z is the Z statistic and can be used to determine the level of significance. When the absolute value of Z is greater than $Z_{1-\alpha/2}$, the null hypothesis is rejected. The significance level selected in this study was α = 0.05. If the Z value is greater than the positive critical value (usually 1.96 with a corresponding significance level of 0.05), the data can be considered to have a significant upward trend. If the Z value is less than a negative critical value (usually, −1.96), a significant downward trend in the data can be considered. If the Z value is within the critical range (i.e., between −1.96 and 1.96), the

null hypothesis cannot be rejected as there is no significant upward or downward trend in the data.

2.6. Evapotranspiration Concentration Index

Evapotranspiration concentration index (ETCI) is an index that characterizes the concentration and seasonality of evapotranspiration during the year. The precipitation concentration index is a statistical measure used to quantify the temporal distribution of precipitation over a specific period (e.g., monthly or annual) [39]. Here, we adopt the concept to quantify the temporal distribution of monthly ET. The annual ETCI is calculated by the following:

$$ETCI = \frac{\sum_{i=1}^{12} ET_i^2}{\left(\sum_{i=1}^{12} ET_i\right)^2} \times 100 \quad (14)$$

where ET_i is the evapotranspiration of the ith month. In practical applications, it can be defined that, when ETCI $\leq$ 10, the monthly distribution of the annual evapotranspiration is more uniform; when 11 $\leq$ ETCI < 20, it indicates that the annual evapotranspiration is seasonal, that is, the annual evapotranspiration has a certain concentration; when ETCI $\geq$ 20, it can be considered that the distribution of annual evapotranspiration in the region is abnormally concentrated during the year, and the monthly variation of evapotranspiration is very large.

3. Results

3.1. The Overall Performance of Nine Datasets

Scatter plots for nine ET data products against observations at all sites are shown in Figure 2. Performance metrics are calculated for each product using observations and presented in Figure 2. The RMSE of the nine products ranges from 24.10 mm/month to 34.43 mm/month, the range of MBE is −5.43~2.41 mm/month, the range of TS is 0.81~0.90, and the range of r is 0.63~0.83. In general, ETMonitor shows the highest agreement with the observations at flux sites, with the highest r value, the lowest RMSE value, and the highest TS value. PML_V2 also achieves a good performance after ETMonitor, ranking second. SiTHv2, ERA5, ERA5-LAND, GLDAS2.1, and GLEAM4.2a rank third to seventh, respectively. TerraClimate and MERRA-2 have the lowest agreement with the observations at flux sites.

3.2. Accuracy Evaluation for Different Land Surface Conditions

The Taylor diagram is used to visually evaluate the accuracy of ET products by comparing them to the observations with different land covers. The land surface types are roughly divided into six types, i.e., cropland, grassland, forest, shrubland, wetland, and desert. The r, RMSE, standard deviation of observation data, and standard deviation of the product data are calculated and presented in Figure 3.

Overall, all products show a high correlation (mostly $r > 0.8$) in grassland and forest, with RMSE values mostly lower than 25 mm/month. Except for TerraClimate and GLDAS-2.1, the r of other products in the wetland is greater than 0.7, and the RMSE is less than 30 mm/month. The r in the cropland is between 0.6 and 0.85, and the RMSE is between 25 and 40 mm/month, showing a moderate performance. The RMSE in the desert is the lowest, meanwhile, its r value is almost the lowest ($r < 0.6$). The r value of the shrub is also low, mostly less than 0.6, whereas the RMSE value is mostly greater than 30 mm/month, and the overall performance is only slightly better than that of the desert. Except in the desert, ETMonitor shows a relatively stable good performance, followed by SiTHv2.

TerraClimate and MERRA-2 present the lowest agreement with flux observations in almost all land types. GLEAM4.2a and GLDAS-2.1 perform slightly better than TerraClimate.

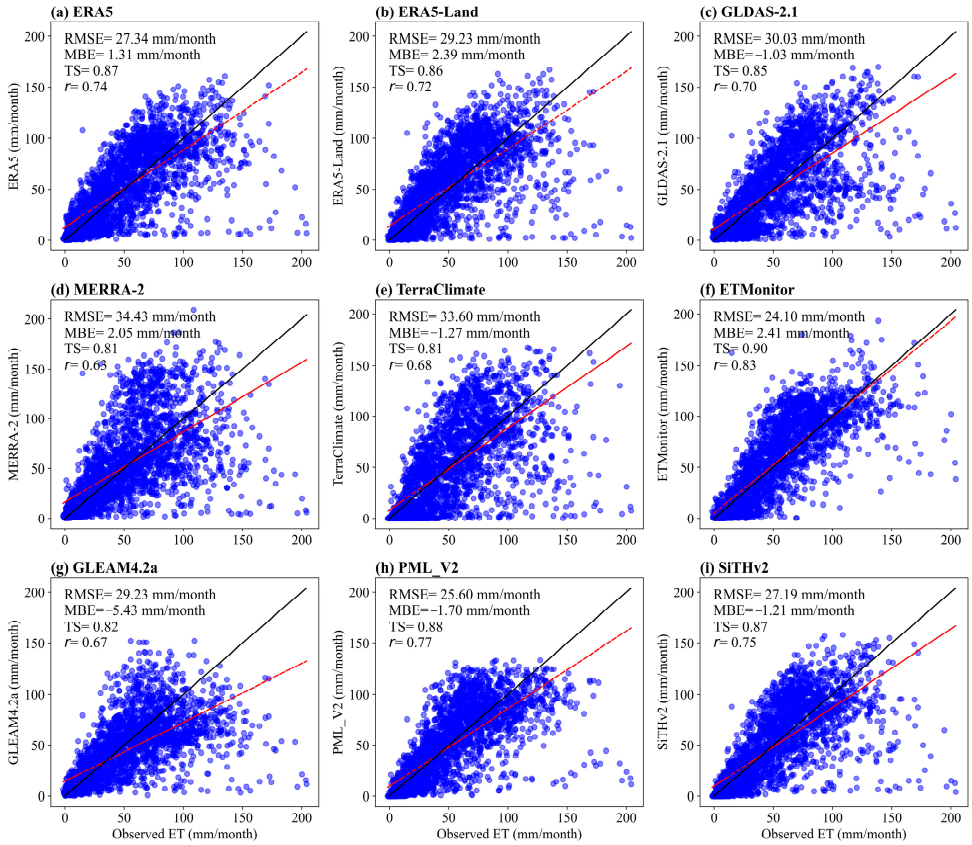


Figure 2. The accuracy assessment results and corresponding scatter plots for the nine evapotranspiration products, derived from observations at all 40 flux tower sites.

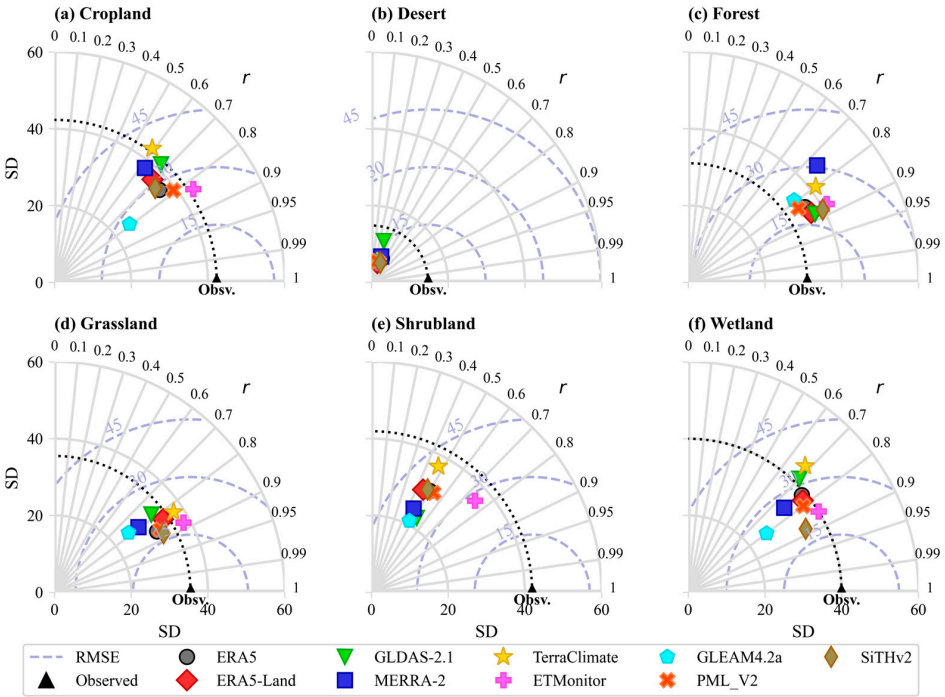


Figure 3. Taylor diagram of site data and product data based on different underlying surface types.

The accuracy of ET products exhibits notable variation across land cover types, with forests generally showing higher correlation coefficients due to strong and stable ET signals, dense vegetation cover, well-parameterized models, and abundant flux observations. In contrast, deserts tend to yield lower correlations owing to weak ET signals, higher susceptibility to noise, limited model performance under arid conditions, and sparse, less representative flux tower data.

3.3. Performance of Nine Datasets in Different Subregions

The heat maps of the performance of each product relative to the observation data at sites in four geographical regions are shown in Figure 4. As far as MBE is concerned, in northern China, all products perform well, all MBE is less than 10 mm/month, and most MBE is less than 6.5 mm/month. In the southern region, most products perform poorly, and the MBE of MERRA-2 is as high as 29.96 mm/month. As far as RMSE is concerned, all products perform well in the Tibetan plateau region, and RMSE is less than 32 mm/month, but most of the performance in the northwest region is not good. Only ETMonitor plays a stable role, and RMSE is maintained at a good level of 25.60 mm/month. As far as *r* is concerned, all products perform well in the Tibetan plateau region, most of the *r* values are higher than 0.85, and the performance in the northern region is relatively good. The *r* values of most products are greater than 0.75, but the overall performance in the northwest region is poor. Except that the ETMonitor is still stable, the *r* value is as high as 0.84, and the *r* values of other products are less than 0.70. As far as TS is concerned, all products perform well in the northern region.

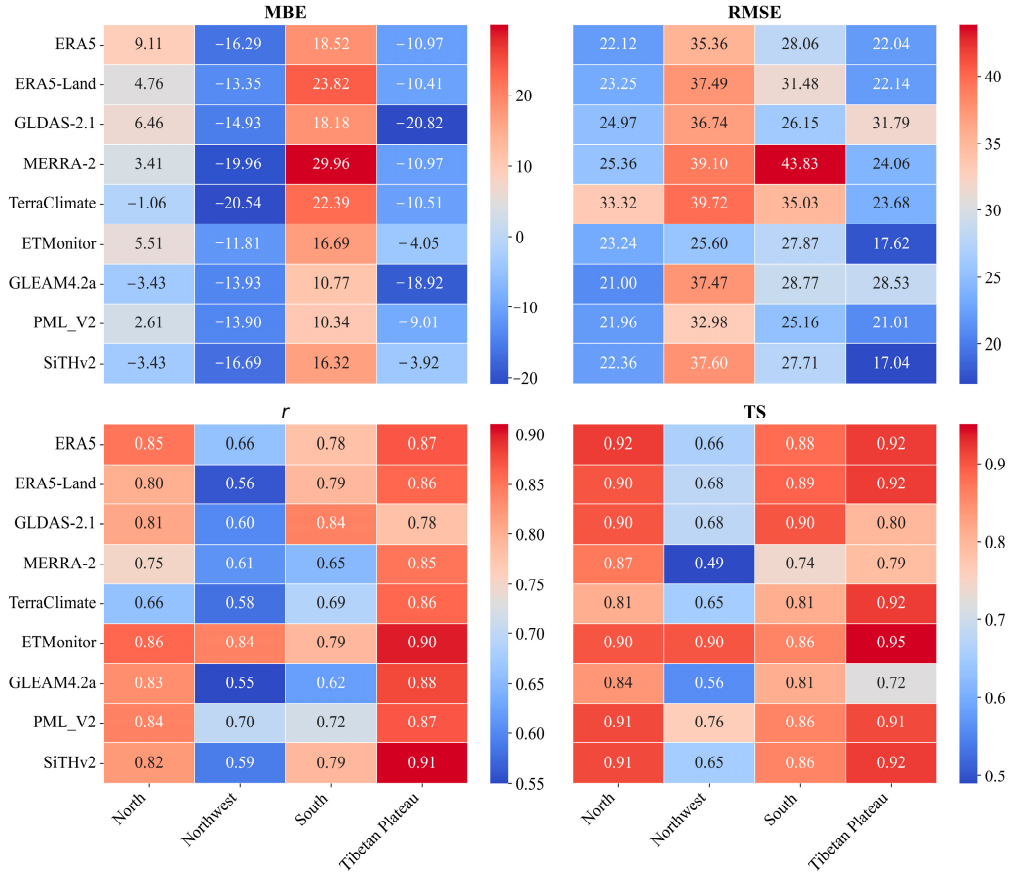


Figure 4. Heat map of product evaluation metrics in different geographical regions. The units of MBE and RMSE are both mm/month.

3.4. Comparison of Seasonal Variations of Different ET Products

The monthly averages of all products in different regions are shown in Figure 5. In general, all products can correctly reflect the seasonal variation of ET. However, all products underestimate ET in the northwest region and overestimate ET in the southern part of China throughout the year. In the northern region, most products overestimate ET in summer and early autumn (June~September). In the Tibetan plateau region, ET values by most products are mostly undervalued, except for the ETMonitor. The climatic characteristics and environmental conditions of different regions have a significant impact on evapotranspiration, and different ET products may not fully consider the unique climatic and environmental factors in these regions. For example, in the northern region, especially in the cold winter and dry spring and autumn, the evapotranspiration of plants is relatively low. If the product model ignores the moisture limit in winter or relies too much on temperature and sunshine duration to estimate evapotranspiration, it is prone to overestimation. However, the northwest region is generally dry, soil moisture is low, and precipitation is very limited, which directly affects the actual performance of ET. The production of evapotranspiration is not only affected by temperature and sunlight, but also limited by soil moisture and water available to vegetation. In such areas, the product model may be oversimplified and fail to take full account of the soil water limit and water use efficiency of plants, resulting in an underestimation of evapotranspiration. The southern region usually has higher temperatures, sufficient precipitation, and vigorous vegetation growth, which means that ET is generally higher in these regions. However, if ET products ignore local precipitation differences or rely too much on meteorological data (such as temperature and humidity), it will lead to the overestimation of ET. This may be caused by being too optimistic about the water supply in the southern region by ET models. The calculation of evapotranspiration in the Tibetan plateau is more complicated because of its unique geographical environment (high altitude, low temperature, special plant community, etc.). At high altitudes, the air is thin, the temperature is low, the plant growth cycle is short, and the evapotranspiration is low. ET products may not effectively capture these special environmental conditions, especially the effects of altitude changes on temperature and humidity, leading to underestimation.

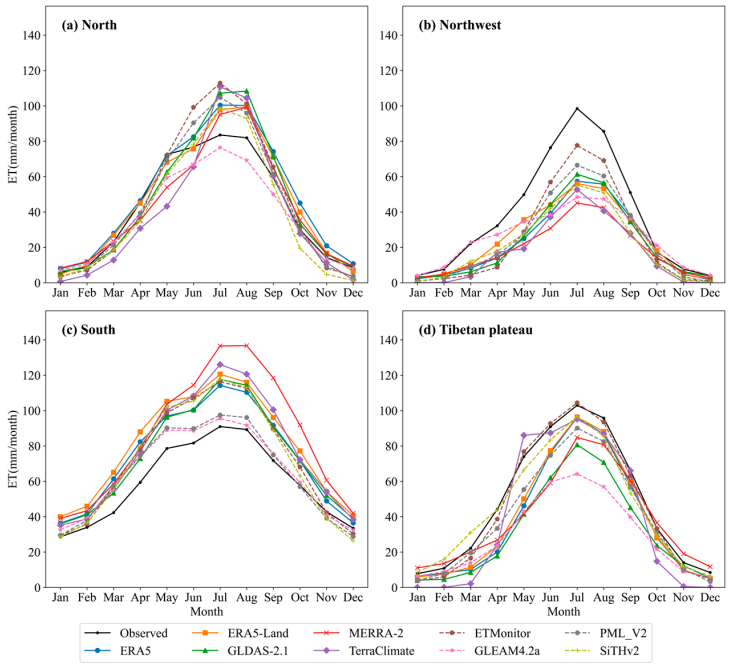


Figure 5. A line chart of seasonal changes based on product data from different regions.

3.5. Improving ET Data by Merging the Best Products Using TCA

The three product datasets with the overall best performance, namely, ETMonitor, PML_V2, and SiTHv2, are selected for data fusion using the Triple Collocation Analysis (TCA) method (the merged data are referred to as TCA_ET hereafter). The accuracy evaluation results for TCA_ET are shown in Table 2. TCA_ET performs much better than the original three datasets in terms of MBE, but, on the whole, no better than ETMonitor in terms of RMSE, r, and TS, although better than the other two products. We also compared TCA_ET with the original datasets in different regions, as shown in Table 3. Except for the southern region, TCA_ET does not outperform ETMonitor, although it is better than the other two datasets in all four regions. The relatively limited improvement in the accuracy of the TCA_ET, as compared to ETMonitor, can be attributed to the nature of the TCA method. While TCA effectively reduces uncorrelated random errors across multiple datasets, it assigns weights based on statistical error covariance rather than absolute accuracy. Consequently, the high precision of ETMonitor may be diluted by the relatively lower-quality inputs from PML_V2 and SiTHv2, particularly in regions where they exhibit systematic biases. The results indicate that the improvement with TCA data fusion is marginal. Therefore, it is recommended to use ETMonitor to study evapotranspiration in China instead of taking the data fusion approach.

Table 2. Comparing the accuracy of TCA fusion data with original ET products using all flux observations.

Product	MBE (mm/month)	RMSE (mm/month)	*r*	TS
ETMonitor	2.41	24.10	0.83	0.90
PML_V2	−1.70	25.60	0.77	0.88
SiTHv2	−1.21	27.19	0.75	0.87
TCA_ET	−0.45	24.99	0.79	0.89

Table 3. Comparing the coefficient of correlation (*r*) of TCA fusion data with original ET products based on flux observations in different regions.

Product	North	Northwest	South	Tibetan Plateau
ETMonitor	0.86	0.84	0.79	0.90
PML_V2	0.84	0.70	0.72	0.87
SiTHv2	0.82	0.59	0.79	0.91
TCA_ET	0.84	0.71	0.80	0.90

3.6. Spatial and Temporal Variations of Evapotranspiration in China Revealed by Different Data Products

Figure 6 shows the spatial variability of the multi-year mean ET of different ET products in China from 2001 to 2020. As expected, the annual evapotranspiration of the nine products exhibits a similar spatial pattern, all increasing from northwest to southeast. A remarkable feature of the spatial pattern is that the ET values of MERRA-2 and TerraClimate are significantly larger than those of others in the southeastern parts of China.

Figure 7 shows the boxplots of multi-year mean ET values of all grids by different ET products. By visual inspection, the medians of most products are close to each other, but the median of GLEAM4.2a is the lowest. ERA5-Land has the largest multi-year average evapotranspiration (504.8 mm/yr) in China during the period from 2001 to 2020, followed by MERRA-2 (498.7 mm/yr), ERA5 (497.5 mm/yr), SiTHv2 (458.4 mm/yr), GLDAS-2.1 (448.7 mm/yr), ETMonitor (442.5 mm/yr), PML_V2 (434.7 mm/yr), and TerraClimate (432.7 mm/yr), and GLEAM4.2a has the smallest estimate (397.8 mm/yr), which means that the average ET estimate by reanalysis datasets (476 mm/yr) is approximately 10%

larger than that by remote sensing datasets (433 mm/yr). Remote sensing products have more outliers than reanalysis products. While there are no missing data for ETMonitor, SiTHv2, ERA5, and ERA5-Land, a lot of missing values are present in some parts of the northwest and south for PML_V2 due to its use of MODIS albedo, emissivity, leaf area index (LAI), and other data as input, which exhibit many missing values.

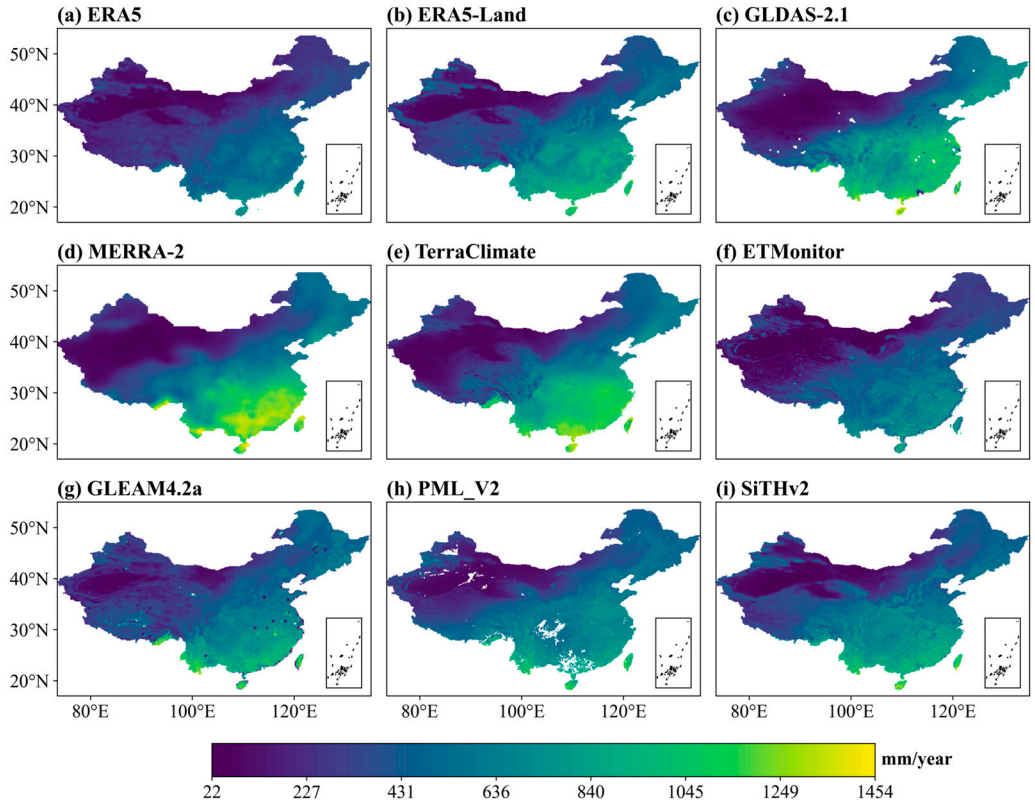


Figure 6. Spatial distribution of multi-year average evapotranspiration in China from 2001 to 2020.

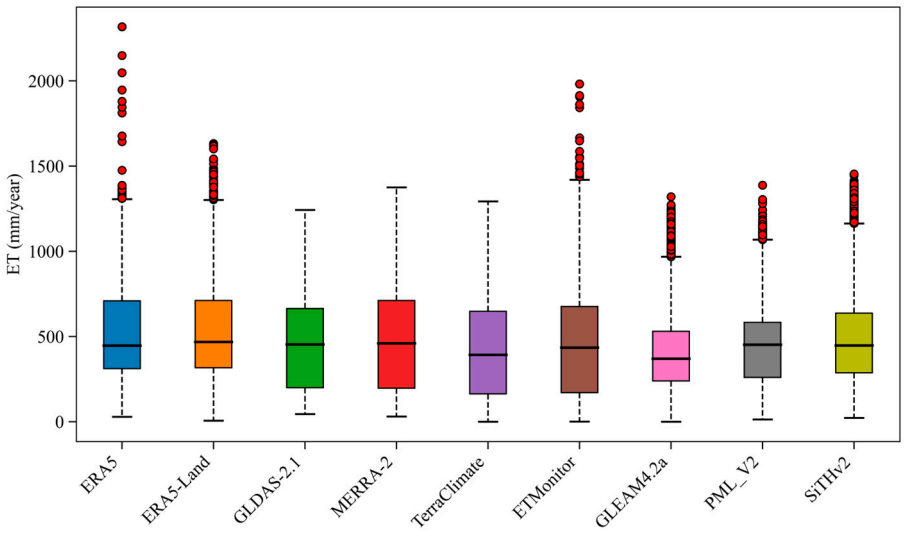


Figure 7. Boxplots of multi-year average evapotranspiration in China from 2001 to 2020. (The bottom side of the box is the first quartile (Q1), the upper side is the third quartile (Q3), and the middle line is the median (Q2). The lines on both sides of the box represent the range of minimum and maximum values in the data, except for outliers, and the outliers are represented by red dots here).

Figure 8 shows the spatial distribution of the Z values of the MK trend test for different ET products in China from 2001 to 2020. The detected trends by different products exhibit quite different spatial patterns. Among them, the trend changes of ERA5 and ERA5-Land are similar, showing a significant upward trend in some parts of northern China, some parts of the Tibet Plateau, and some parts of southern China, while the rest show a significant downward trend. GLDAS-2.1 and ETMonitor showed a significant increase in the northern and northwestern regions, while GLEAM4.2a and PML_V2 showed a significant decrease in most of the northwestern regions and some of the southern regions. TerraClimate and SiTHv2 both showed a significant declining trend in the southern region, while MERRA-2 showed a significant increasing trend in most regions of China. To obtain an overall spatial trend, the average Z values and standard deviations of the MK trend test for nine ET products in China from 2001 to 2020 are calculated and shown in Figure 9. Intuitively, Figure 9a shows that there is a significant increasing trend in most parts of northeast China, whereas, in most parts of the Yangtze River basin in the east, Xinjiang Province in the northwest, and the Tibetan Plateau in the south exhibit slight decreases in ET in terms of Z values. However, only the increasing trend in northeast China is significant, with Z values greater than 1.96 (i.e., $\alpha = 0.05$). It can also be seen from Figure 9b that the standard deviation of some parts of the northeast, some parts of Xinjiang Province, and some parts of the Yangtze River basin in the east is smaller, that is, the data are more concentrated on the mean, reflecting the fact that different data trends in these regions may be consistent.

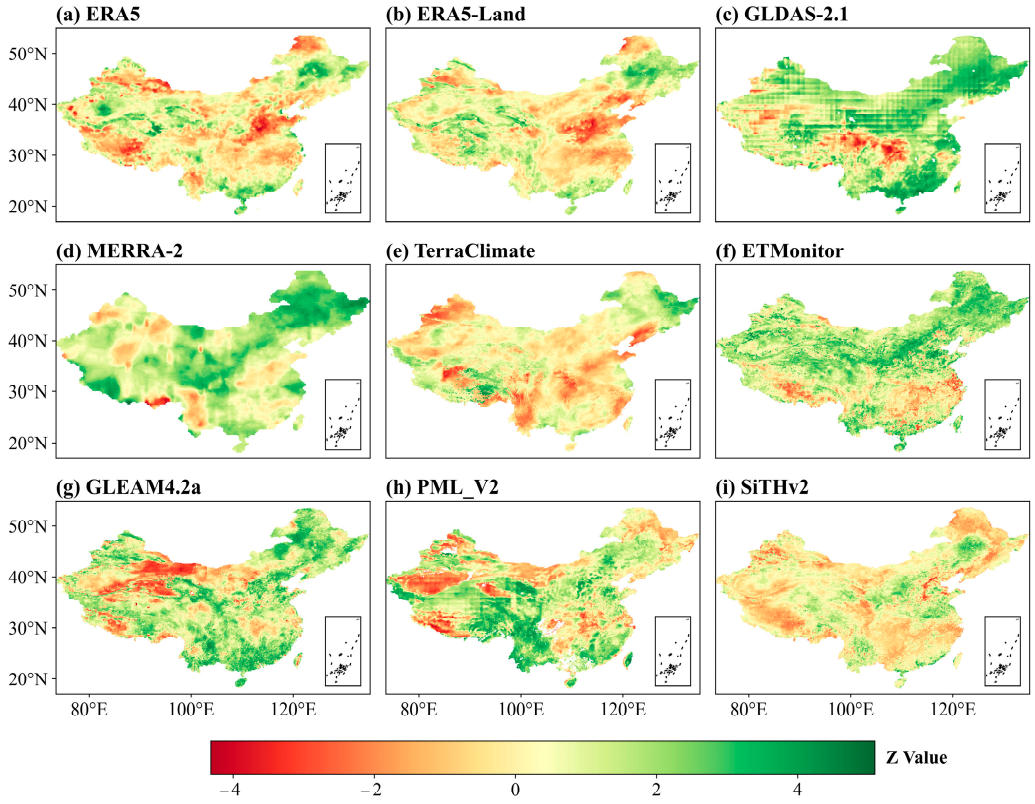


Figure 8. Spatial distribution of Z values of MK trend test for ET in China from 2001 to 2020.

Variations in the annual average ET by different products from 2001 to 2020 are presented in Figure 10. By visual inspection, we know that the average ET exhibits an increasing trend generally, except for ERA5 and ERA5-Land. Further investigation results with the MK trend test are presented in Table 4, which shows that five datasets (i.e., GLDAS-2.1, MERRA-2, ETMonitor, GLEAM4.2a, and PML_V2) indicate a significant

increase in ET during 2001–2020, whereas only ERA5 indicates an opposite trend. (The significance level selected here is $\alpha = 0.05$.)

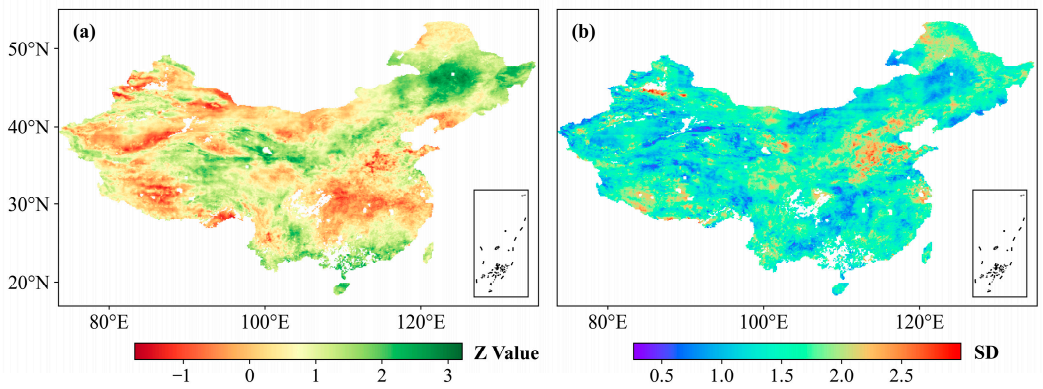


Figure 9. Average Z values (**a**) and their standard deviation (**b**) of MK trend test for nine ET products in China from 2001 to 2020.

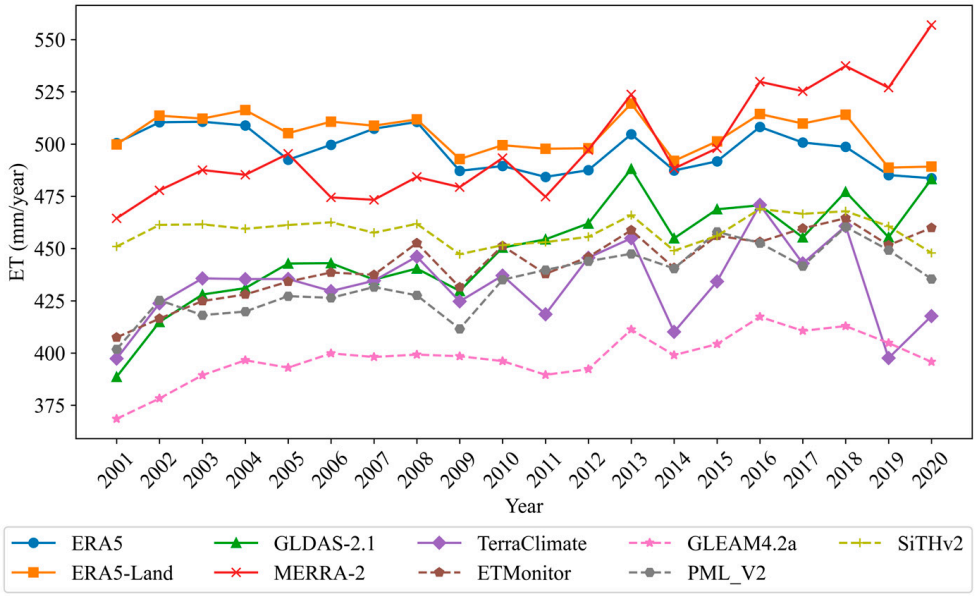


Figure 10. Time series of areal average annual evapotranspiration in China from 2001 to 2020.

Table 4. MK trend test of real average annual evapotranspiration and evapotranspiration concentration index in China from 2001 to 2020. An asterisk (*) indicates statistical significance at the 0.05 level.

Product	Trend		Z		Slope	
	ET	ETCI	ET	ETCI	ET	ETCI
ERA5	decreasing	no trend	−2.30 *	1.91	−0.72 mm/year	0.03
ERA5-Land	no trend	no trend	−1.40	1.40	−0.63 mm/year	0.02
GLDAS-2.1	increasing	no trend	4.57 *	−0.88	3.28 mm/year	−0.01
MERRA-2	increasing	no trend	3.99 *	−1.65	3.71 mm/year	−0.03
TerraClimate	no trend	no trend	0.75	−1.20	0.83 mm/year	−0.04
ETMonitor	increasing	no trend	4.51 *	−0.88	2.36 mm/year	−0.03
GLEAM4.2a	increasing	no trend	3.02 *	−0.49	1.36 mm/year	−0.01
PML_V2	increasing	increasing	4.19 *	3.80 *	2.18 mm/year	0.07
SiTHv2	no trend	increasing	0.42	1.98 *	0.17 mm/year	0.02

It can be seen from Figure 11 that the multi-year average evapotranspiration of different products shows a longitudinal gradient of about 8.2~14.5 mm/year/degree, increasing from 80°E to 120°E in the 30°N~45°N latitude zone. Generally, reanalysis datasets have larger gradients than the remote sensing products, among which MERRA-2 has the largest gradient (14.5 mm/year/degree) and GLEAM4.2a has the smallest gradient (8.2 mm/year/degree). The multi-year average evapotranspiration of different products in the 100°E~120°E longitude band exhibits a longitudinal gradient of about −45.7~−23.0 mm/year/degree decreasing from 20°N~42°N. Similar to the case of longitudinal gradient, the reanalysis datasets have larger longitudinal gradients than the remote sensing products, with the gradient of MERRA-2 being the largest (−45.7 mm/year/degree), and the gradient of GLEAM4.2a being the smallest (−23.0 mm/year/degree). There are some outliers in GLEAM4.2a at low latitudes, which is an indication of the presence of some abnormalities close to the southern borders of China.

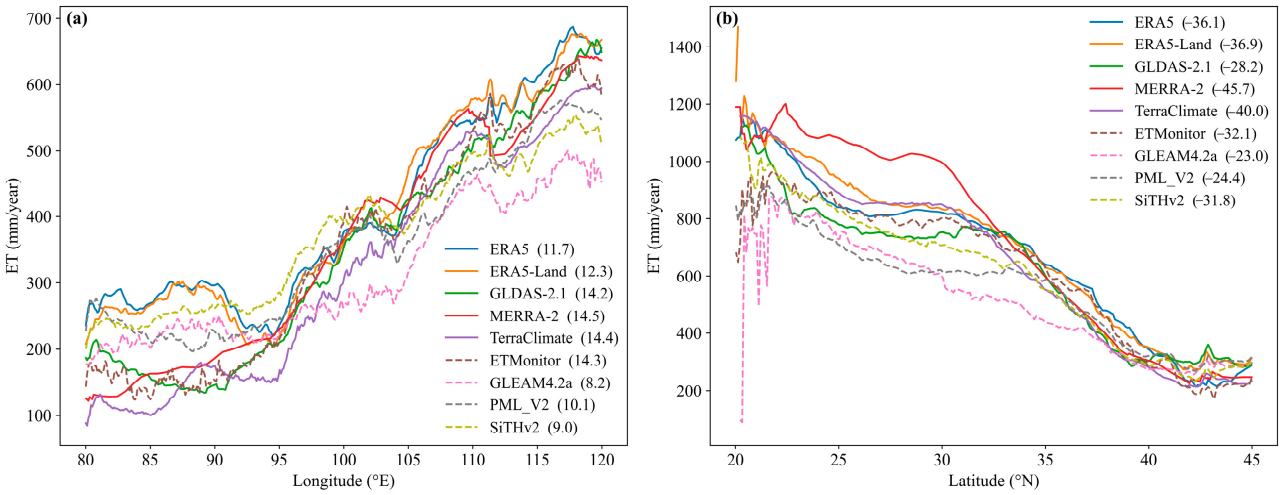


Figure 11. (**a**) The 30°N~45°N latitude zone from 80°E~120°E interval by longitude average change process line of ET in China from 2001 to 2020. (**b**) The 100°E~120°E longitude zone from 20°N~45°N latitudinal mean change process line of ET in China from 2001 to 2020. The numbers in the brackets in the legend represent their respective slopes, and the unit is mm/year/degree.

To investigate the change in seasonality of the ET products, we calculate the evapotranspiration concentration index (ETCI) in each year from 2001 to 2020. It can be seen from Figure 12 that the multi-year average ETCI over China from 2001 to 2020 is generally larger in the northwest parts than in the southeast parts. Variations of the annual ETCI of all the products are shown in Figure 13. The annual values of ETCI by most products vary between 12 and 20. TerraClimate has the overall highest ETCI, indicating the presence of the strongest seasonality, followed by ETMonitor, and GLEAM4.2a has the lowest ETCI. Most products have no significant trend in ETCI, whereas PML_V2 and SiTHv2 exhibit an increasing trend. Further investigation with the MK trend test confirms such trends (listed in Table 4).

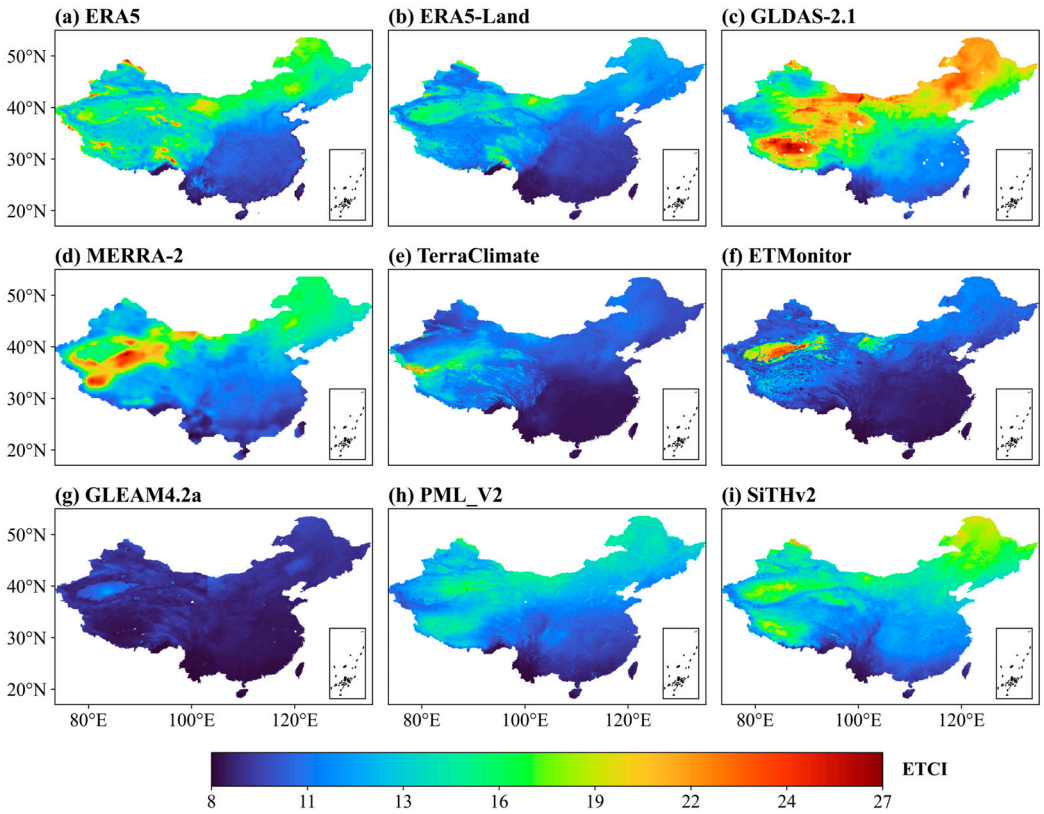


Figure 12. Spatial distribution of ET concentration index (ETCI) in China from 2001 to 2020.

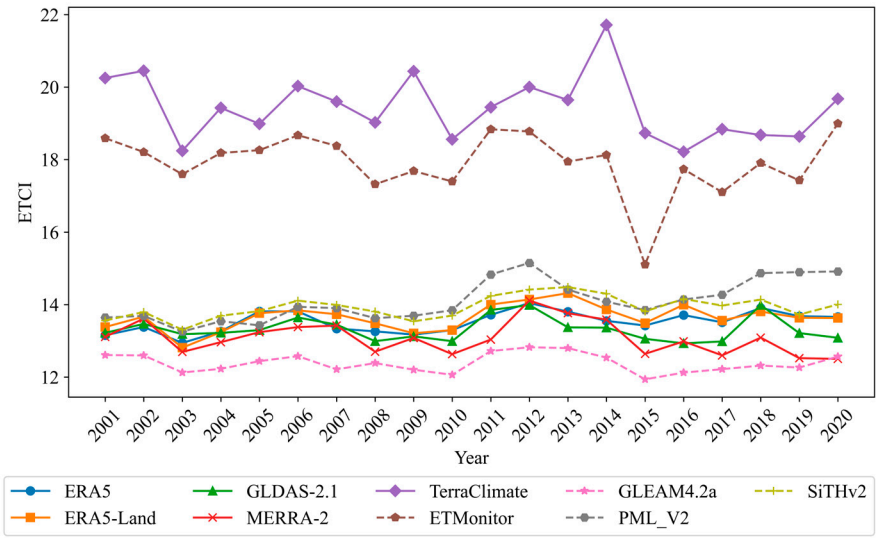


Figure 13. Variations of annual ET concentration index (ETCI) by different datasets in China from 2001 to 2020.

4. Discussion

4.1. Comparative Analysis with Some Recent Evaluation Results in the Literature

With more and more evapotranspiration products published or updated, the evaluation of those products has been conducted for different regions of the world by many researchers in the last decade. Here, we would like to compare our evaluation results with several results recently published, shown in Table 5, in the past two years. Zuo et al. [23] evaluate six evapotranspiration products based on eight flux observation stations in China and show that, in general, all ET products show satisfactory performance. The RMSEs of

ERA5-Land, GLEAM, and PML_V2 are all lower than 30 mm/month, which is consistent with our research situation. However, since the number of observation stations used in our study is much more than that of Zuo et al. [23], only the r of PML_V2 is above 0.75 under such circumstances. The performance of ERA5-Land in our study is generally better than that of GLEAM, which is slightly inconsistent with the conclusion of Zuo et al. [23], presumably due to the insufficient number of observation stations used in Zuo et al.'s study.

Table 5. The accuracy evaluation results of different evapotranspiration product data in the literature over the past two years.

Reference	Evaluation Region	Number of Stations	Product Name	Evaluation Result
Zuo et al. [23]	China	8	ERA5-Land, GLASS, GLDAS, GLEAM, PML_V2, SSEBop	The accuracy of GLASS, GLEAM and PML_V2 is higher than other products.
Shi et al. [22]	China	9	AVHRR, GLASS, GLEAM, IDAHO, MOD16, PML_V2	GLEAM and PML_V2 perform better than other products, and PML_V2 performs better than GLEAM.
Yao et al. [17]	China	12	GLEAMv3.5a, GLDASv2.0, GLDASv2.1, CR, CFET, NTSG, PML_V1	The GLEAMv3.5a product performs better in the inter-annual AET distribution, but lower in the spatial pattern.
Xie et al. [15]	Globe	230	GLASS-AVHRR, GLASS-MODIS, BESS, FLUXCOM, GLEAMv3a, MOD16A2, PML_V2, ERA5, MERRA-2	FLUXCOM, PML_V2 and GLASS-MODIS outperform other products.
Qian et al. [16]	Globe	153	CLSM, FLDAS, NOAH, ERA5, GLEAMv3.6b, MOD16A2, PML_V2, REA, Synthesized	GLEAM_v3.6b has the highest accuracy, ERA5 is better, and PML_V2 has relatively poor accuracy.
Liu et al. [21]	Globe	206	MOD16, NTSG, PT-JPLSM, SSEBop, GLEAM, GLDAS, FLDAS, TerraClimate, FLUXCOM, SynthesisET	The product performance of GLEAM is in the middle level, while the product accuracy of TerraClimate is the lowest.

In our study, the RMSEs of GLEAM and PML_V2 are both lower than 30 mm/month, and the performance of PML_V2 is indeed better than GLEAM, which is consistent with the study of Shi et al. [22]. Yao et al. [17] believe that GLEAM performs well in the inter-annual AET distribution but poorly in the spatial pattern. In our study, GLEAM's performance in the northern and Tibetan Plateau regions is much better than that in the northwestern and southern regions, indicating the benefits of regional evaluation. Xie et al. [15] believe that, in general, FLUXCOM, PML_V2, and GLASS-MODIS are superior to other products. This is consistent with the conclusion that the performance of PML_V2 is indeed superior.

Qian et al. [16] believe that GLEAM_v3.6b has the highest accuracy, ERA5 performs better, and PML_V2 has relatively poor estimation accuracy, which is inconsistent with our study, showing that the performance of PML_V2 is better than that of ERA5 and that of ERA5 is better than that of GLEAM4.2a. This result should be caused by the differences between the version of data used and the flux observation stations. Compared with GLEAM_v3.6b, GLEAM4.2a introduces several substantial improvements. Notably, it adopts a hybrid learning approach for estimating evaporative stress by integrating

eddy-covariance and sap flow observations [40], enhancing accuracy under water-limited conditions. The model also incorporates an improved representation of rainfall interception, including contributions from short vegetation [41]. Potential evaporation in GLEAM v4.2a is now computed using the Penman equation, which accounts for both radiative and aerodynamic components, instead of the simpler Priestley–Taylor approach. Additionally, the model explicitly includes vegetation access to groundwater [42], improving reliability in ecosystems with shallow water tables. Furthermore, the spatial resolution is enhanced to 0.1°, and the dataset extends over a longer temporal period (1980–2023), offering greater utility for fine-scale and long-term evapotranspiration analysis [32]. These differences may substantially influence the estimation of evapotranspiration, and the use of only eight flux sites in China by Qian et al. [16] could have contributed to the discrepancies observed in the evaluation results. Liu et al. [21] conclude that, in general, GLEAM's product performance remains at an intermediate level among all products, while TerraClimate has the lowest agreement with the observations at flux sites, which is also consistent with the conclusion of our study. All in all, for the study of evapotranspiration product evaluation in China, our study selects sufficient remote sensing data and reanalysis data for comparison, uses the latest data sources and data versions, and collects a lot of flux observation data, which is often rarely performed by other researchers. The updated iteration of the data version and the insufficient data of the flux observation stations usually lead to the one-sidedness of the evaluation results.

4.2. Advantages and Disadvantages of Remote Sensing Products and Reanalysis Products

Our study shows that remote sensing ET products (ETMonitor, PML_V2, and SiTHv2) generally have better performance than reanalysis ET products. In addition, remote sensing products have higher spatiotemporal resolution than reanalysis products. However, due to the limitation of satellite data availability, remote sensing products cannot be produced for a long-term time period, and there is a long time lag. For instance, the best two remote sensing products, ETMonitor and PML_V2, start from 2000 and are available for years no later than 2021 and 2020, respectively. Additionally, these remote sensing products are very likely to present a large number of missing values in a specific region, such as PML_V2. Under the influence of MODIS input data, there are many missing values in some northwestern and some southern regions. Fortunately, none of the flux observation sites used in this study are located in the missing data regions of the PML_V2 product; therefore, the data gaps in PML_V2 do not affect the evaluation results. For short-term evapotranspiration studies in China, ETMonitor can be directly considered as a suitable data source. Compared with remote sensing products, reanalysis products generally have a longer time series and more complete spatial distribution, which makes them more appropriate for long-term climate change research. Although the accuracy of reanalysis products is generally inferior to that of remote sensing data, ERA5-Land and ERA5, which have good accuracy in northern and southern regions of China, can be recommended in long-term climate change research.

4.3. Limitations and Outlook

Theoretically, the reliability of data quality assessments improves with an increased number of flux observation sites. Although this study utilized data at 40 flux towers—substantially more than those employed in most previous regional assessments in China—it must be acknowledged that the spatial representativeness of these stations remains limited given China's vast and diverse territory. Moreover, due to the varied establishment times of flux towers, the temporal length of available flux observations differs across sites, making it challenging to directly compare the spatial patterns of ET trends from

each dataset with observational data. However, the capability of a dataset to accurately capture long-term variability is a critical attribute. Therefore, future studies should aim to improve evaluation methods in this regard, if feasible. Furthermore, the flux observations inevitably contain non-systematic errors. Despite the implementation of rigorous preprocessing steps, issues related to the accuracy of the original data could not be entirely mitigated, which may have introduced some degree of uncertainty into the subsequent analyses. Additionally, the spatial resolutions of the various ET products differ. Although resampling was employed to harmonize these resolutions, some unavoidable uncertainties may still arise due to the scale mismatch. Moreover, the data fusion approach applied in this study warrants further improvement. Different ET products exhibit considerable variability in performance across months and seasons. Incorporating dynamic weighting schemes that reflect these temporal differences could enhance the accuracy of the fused product. Additionally, alternative fusion strategies—such as integrating higher-resolution datasets or employing more sophisticated algorithms like Bayesian optimization—may offer further potential to improve the overall quality and reliability of the results.

5. Conclusions

Accurate estimation of evapotranspiration (ET) is critical for advancing climate and hydrological research. As the primary process linking the water, energy, and carbon cycles, ET directly influences climate feedbacks (e.g., droughts, heatwaves), water resource availability, and ecosystem productivity. However, large uncertainties persist in ET quantification due to differences in model parameterizations, input data, and spatial-temporal resolutions across reanalysis and remote sensing products. Using observational data from flux stations, five reanalysis actual ET datasets (ERA5, ERA5-LAND, GLDAS-2.1, MERRA-2, TerraClimate) and four remote sensing estimation ET datasets (ETMonitor, GLEAM4.2a, PML_V2, SiTHv2) in China from 2001 to 2020 were compared. First, we validated these products and compared their accuracy at the site scale. Then, we attempted to improve data fusion using the TCA method. In addition, we conducted a comprehensive analysis of spatio-temporal patterns of evapotranspiration to identify consistencies and differences among the products across China. The main findings are as follows: (1) The ETMonitor data ranked first in the evaluation in terms of consistency with the observations at 40 flux sites, with the highest *r* and TS, and the lowest RMSE, followed by PML_V2 and SiTHv2. TerraClimate and MERRA-2 have the lowest agreement with flux observations in terms of almost all evaluation metrics. The regional analysis indicates that ETMonitor, ERA5, and PML_V2 are suitable for application in northern China. ETMonitor demonstrates the highest applicability in the northwest, while ETMonitor, SiTHv2, ERA5-Land, and ERA5 are appropriate for use in the southern region. On the Tibetan Plateau, ETMonitor or SiTHv2 appear suitable for application. (2) The TCA method is used to merge the three best-performing remote sensing data products, but the results show that the accuracy improvement with the data fusion approach is limited. (3) The analysis of evapotranspiration from 2001 to 2020 across China reveals distinct patterns in both total ET amounts and seasonal variability. The estimation of the multi-year average evapotranspiration in China during the period from 2001 to 2020 ranges from 397.8 mm/year (GLEAM4.2a) to 504.8 mm/year (ERA5-Land). From 2001 to 2020, annual evapotranspiration in China generally increased, but with varying rates across different products. MERRA-2 showed the largest annual increase rate (3.71 mm/year), while SiTHv2 showed the smallest (0.17 mm/year). Spatially, there is a significant increasing trend in most parts of northeast China, where the average Z value of the MK trend test for nine ET products is greater than 1.96 (i.e., $\alpha = 0.05$) and its standard deviation is also low, reflecting that different data trends in this region are consistent. All products can capture the seasonality of ET in China,

but they tend to underestimate ET in northwest China and overestimate it in southern China throughout the year. There are no significant changes in the seasonality of ET by most ET products, except for PML_V2 and SiTHv2, which indicate an increase in seasonality in terms of the evapotranspiration concentration index. These spatial and seasonal patterns result from the complex interactions between climatic factors, vegetation types, and the inherent characteristics of the ET products. This evaluation informs the selection of reliable evapotranspiration products, offering critical support for climate modeling, hydrological studies, and water resource management.

Author Contributions: Conceptualization, Y.L. and W.W.; methodology, Y.L. and W.W. and Z.H.; software, Y.L., T.Z. and Z.H.; validation, Y.L. and T.Z.; formal analysis, Y.L. and T.Z.; data curation, Y.L. and T.Z.; writing—original draft preparation, Y.L.; writing—review and editing, W.W.; visualization, Y.L.; supervision, W.W.; funding acquisition, W.W. All authors have read and agreed to the published version of the manuscript.

Funding: This research was financially supported by the National Key Research and Development Program of China (grant number 2023YFC3209201) and the National Natural Science Foundation of China (grant number 42471027).

Data Availability Statement: The original contributions presented in the study are included in the article, further inquiries can be directed to the corresponding author.

Conflicts of Interest: The authors declare no conflicts of interest.

Appendix A

Table A1. List of observation data used in this study.

Land Cover	Station Name (Abbreviation)	Longitude/°E	Latitude/°N	Temporal Resolution	Observation Period	Reference
Cropland	Daman Super Station (DMS)	100.37	38.86	30 min	2012–2020	Liu et al. [43,44]
	Gucheng (GC)	115.67	39.13	30 min	2020	Zhou et al. [45]
	Jinzhou (JZ)	121.20	41.15	30 min	2005–2014	Zhang et al. [46]
	Jurong (JR)	119.22	31.81	30 min	2015–2020	Zhou et al. [47]
	Luancheng (LC)	114.68	37.88	30 min	2013–2017	Liu et al. [48]
	Panjin Rice Field Station (PJC)	121.96	40.94	30 min	2018–2020	Jia et al. [49]
	Yucheng (YC)	116.57	36.83	30 min	2003–2010	Zhao et al. [50]
	Changling Rice Field Station (CLC)	123.47	44.60	30 min	2018–2020	Dong et al. [51]
Desert	Desert Station (DS)	100.99	42.11	30 min	2015–2020	Liu et al. [43,44]
Forest	Ailaoshan (ALS)	101.03	24.54	Monthly	2009–2013	Qi et al. [52]
	Baotianman (BTM)	111.94	33.50	30 min	2017–2018	Niu et al. [53]
	Danzhou Rubber Forest Station (DZRF)	109.48	19.55	Monthly	2010–2018	Yang et al. [54]
	Dinghushan (DHS)	112.53	23.17	30 min	2003–2010	Li et al. [55]
	Huzhong (HZ)	121.02	51.78	30 min	2014–2018	Yan et al. [56]
	Jinfoshan National Station (JFSN)	107.15	29.02	30 min	2020	Tang et al. [57]
	PuDing (PD)	106.32	26.60	30 min	2015–2019	Wang et al. [58]
	Qianyanzhou (QYZ)	115.07	26.73	30 min	2003–2010	Dai et al. [59]
	Xishuangbanna (XSBN)	101.21	21.96	Monthly	2003–2015	Qi et al. [60] Liu et al. [61]
	Xishuangbanna Rubber Forest Station (XSBNRF)	101.27	21.90	30 min	2010–2014	Yu et al. [62]
	Xiaolangdi (XLD)	112.47	35.03	30 min	2016–2017	Huang et al. [63]
	Yanshan artificial coniferous forest station (YSF)	116.66	40.42	30 min	2020	Du et al. [64]
	Changbaishan (CBS)	128.10	42.40	30 min	2003–2010	Wu et al. [65]

Table A1. *Cont.*

Land Cover	Station Name (Abbreviation)	Longitude/°E	Latitude/°N	Temporal Resolution	Observation Period	Reference
Grassland	Arou Super Station (ARS)	100.46	38.05	30 min	2013–2020	Liu et al. [43] Che et al. [66]
	Damao (DM)	110.33	41.64	30 min	2015–2018	Song et al. [67]
	Dangxiong (DX)	91.08	30.85	30 min	2004–2010	Chai et al. [68]
	Haibei Grassland Station (HBG)	101.31	37.61	30 min	2015–2020	Zhang et al. [69]
	Duolun (DL)	116.28	42.05	30 min	2006–2015	You et al. [70]
	Inner Mongolia (NMG)	116.40	43.33	30 min	2003–2010	Hao et al. [71]
	Xilinhaote (XLHT)	116.67	43.55	30 min	2006–2015	Wang et al. [72]
	Ruoergai (REG)	102.55	32.80	30 min	2015–2020	Chen et al. [73]
	Three River Source Station (TRS)	100.70	35.25	30 min	2012–2016	He et al. [74]
	Yuanjiang (YJ)	102.18	23.47	30 min	2013–2015	Qi et al. [75]
Shrubland	Haibei Shrubland Station (HBS)	101.33	37.67	30 min	2003–2020	Zhang et al. [76] Zhang et al. [77]
	Yanchi Station (YCS)	107.23	37.71	30 min	2012–2016	Han et al. [78]
	Sidaoqiao Super Station (SDQS)	101.14	42.00	30 min	2013–2020	Liu et al. [43,44]
	Yanshan Shrubland Station (YSS)	116.65	40.42	30 min	2020	Du et al. [64]
Wetland	Quanjiao (QJ)	118.25	31.97	30 min	2017–2020	Zhang et al. [79]
	Haibei Wetland Station (HBW)	101.32	37.60	30 min	2004–2009	Zhang et al. [80]
	Yellow River Delta Station (YRD)	118.98	37.77	30 min	2011–2018	Wei et al. [81]
	Panjin Reed Wetland Station (PJRW)	121.96	40.93	30 min	2018–2020	Jia et al. [49]

References

1. Konapala, G.; Mishra, A.K.; Wada, Y.; Mann, M.E. Climate Change Will Affect Global Water Availability through Compounding Changes in Seasonal Precipitation and Evaporation. *Nat. Commun.* **2020**, *11*, 3044. [CrossRef] [PubMed]
2. Padrón, R.S.; Gudmundsson, L.; Decharme, B.; Ducharne, A.; Lawrence, D.M.; Mao, J.; Peano, D.; Krinner, G.; Kim, H.; Seneviratne, S.I. Observed Changes in Dry-Season Water Availability Attributed to Human-Induced Climate Change. *Nat. Geosci.* **2020**, *13*, 477–481. [CrossRef]
3. Oki, T.; Kanae, S. Global Hydrological Cycles and World Water Resources. *Science* **2006**, *313*, 1068–1072. [CrossRef] [PubMed]
4. Zhang, J.; Zhou, X.; Yang, S.; Ao, Y. Spatiotemporal Variations in Evapotranspiration and Their Driving Factors in Southwest China between 2003 and 2020. *Remote Sens.* **2023**, *15*, 4418. [CrossRef]
5. Bai, J.; Wu, G.; Mao, Y. Significant Disparity in Spatiotemporal Changes of Terrestrial Evapotranspiration across Reanalysis Datasets in China from 1982 to 2020. *Remote Sens.* **2023**, *15*, 4522. [CrossRef]
6. Liou, Y.-A.; Kar, S. Evapotranspiration Estimation with Remote Sensing and Various Surface Energy Balance Algorithms—A Review. *Energies* **2014**, *7*, 2821–2849. [CrossRef]
7. Kimball, J.; Running, S. A Review of Remote Sensing Based Actual Evapotranspiration Estimation: A Review of Remote Sensing Evapotranspiration. *Wiley Interdiscip. Rev. Water* **2016**, *3*, 834–853. [CrossRef]
8. Martens, B.; Miralles, D.G.; Lievens, H.; van der Schalie, R.; de Jeu, R.A.M.; Fernández-Prieto, D.; Beck, H.E.; Dorigo, W.A.; Verhoest, N.E.C. GLEAM v3: Satellite-Based Land Evaporation and Root-Zone Soil Moisture. *Geosci. Model. Dev.* **2017**, *10*, 1903–1925. [CrossRef]
9. Zhang, Y.; Kong, D.; Gan, R.; Chiew, F.H.S.; McVicar, T.R.; Zhang, Q.; Yang, Y. Coupled Estimation of 500 m and 8-Day Resolution Global Evapotranspiration and Gross Primary Production in 2002–2017. *Remote Sens. Environ.* **2019**, *222*, 165–182. [CrossRef]
10. Zheng, C.; Jia, L.; Hu, G. Global Land Surface Evapotranspiration Monitoring by ETMonitor Model Driven by Multi-Source Satellite Earth Observations. *J. Hydrol.* **2022**, *613*, 128444. [CrossRef]
11. Bhattarai, N.; Wagle, P. Recent Advances in Remote Sensing of Evapotranspiration. *Remote Sens.* **2021**, *13*, 4260. [CrossRef]
12. Hersbach, H.; Bell, B.; Berrisford, P.; Hirahara, S.; Horányi, A.; Muñoz-Sabater, J.; Nicolas, J.; Peubey, C.; Radu, R.; Schepers, D.; et al. The ERA5 Global Reanalysis. *Q. J. R. Meteorol. Soc.* **2020**, *146*, 1999–2049. [CrossRef]
13. Rodell, M.; Houser, P.R.; Jambor, U.; Gottschalck, J.; Mitchell, K.; Meng, C.-J.; Arsenault, K.; Cosgrove, B.; Radakovich, J.; Bosilovich, M.; et al. The Global Land Data Assimilation System. *Bull. Am. Meteorol. Soc.* **2004**, *85*, 381–394. [CrossRef]

14. Gelaro, R.; McCarty, W.; Suárez, M.J.; Todling, R.; Molod, A.; Takacs, L.; Randles, C.A.; Darmenov, A.; Bosilovich, M.G.; Reichle, R.; et al. The Modern-Era Retrospective Analysis for Research and Applications, Version 2 (MERRA-2). *J. Clim.* **2017**, *30*, 5419–5454. [CrossRef]
15. Xie, Z. Evaluation of Seven Satellite-Based and Two Reanalysis Global Terrestrial Evapotranspiration Products. *J. Hydrol.* **2024**, *630*, 130649. [CrossRef]
16. Qian, L. High Uncertainty of Evapotranspiration Products under Extreme Climatic Conditions. *J. Hydrol.* **2023**, *626*, 130332. [CrossRef]
17. Yao, T.; Lu, H.; Yu, Q.; Feng, S.; Xue, Y.; Feng, W. Uncertainties of Three High-Resolution Actual Evapotranspiration Products across China: Comparisons and Applications. *Atmos. Res.* **2023**, *286*, 106682. [CrossRef]
18. Salazar-Martínez, D.; Holwerda, F.; Holmes, T.R.H.; Yépez, E.A.; Hain, C.R.; Alvarado-Barrientos, S.; Ángeles-Pérez, G.; Arredondo-Moreno, T.; Delgado-Balbuena, J.; Figueroa-Espinoza, B.; et al. Evaluation of Remote Sensing-Based Evapotranspiration Products at Low-Latitude Eddy Covariance Sites. *J. Hydrol.* **2022**, *610*, 127786. [CrossRef]
19. Yu, X.; Qian, L.; Wang, W.; Hu, X.; Dong, J.; Pi, Y.; Fan, K. Comprehensive Evaluation of Terrestrial Evapotranspiration from Different Models under Extreme Condition over Conterminous United States. *Agric. Water Manag.* **2023**, *289*, 108555. [CrossRef]
20. Elnashar, A.; Wang, L.; Wu, B.; Zhu, W.; Zeng, H. Synthesis of Global Actual Evapotranspiration from 1982 to 2019. *Earth Syst. Sci. Data* **2021**, *13*, 447–480. [CrossRef]
21. Liu, H. Intercomparison and Evaluation of Ten Global ET Products at Site and Basin Scales. *J. Hydrol.* **2023**, *617*, 128887. [CrossRef]
22. Shi, X. The Intercomparison of Six 0.1° × 0.1° Spatial Resolution Evapotranspiration Products across Mainland China. *J. Hydrol.* **2024**, *633*, 130949. [CrossRef]
23. Zuo, L.; Zou, L.; Xia, J.; Zhang, L.; Cao, H.; She, D. Multi-Scale Analysis of Six Evapotranspiration Products across China: Accuracy, Uncertainty and Spatiotemporal Pattern. *J. Hydrol.* **2025**, *650*, 132516. [CrossRef]
24. Li, S.; Wang, G.; Sun, S.; Chen, H.; Bai, P.; Zhou, S.; Huang, Y.; Wang, J.; Deng, P. Assessment of Multi-Source Evapotranspiration Products over China Using Eddy Covariance Observations. *Remote Sens.* **2018**, *10*, 1692. [CrossRef]
25. Huang, L.; Steenhuis, T.S.; Luo, Y.; Tang, Q.; Tang, R.; Zheng, J.; Shi, W.; Qiao, C. Revisiting Daily MODIS Evapotranspiration Algorithm Using Flux Tower Measurements in China. *Earth Space Sci.* **2021**, *8*, e2021EA001818. [CrossRef]
26. Burnett, M.W.; Quetin, G.R.; Konings, A.G. Data-Driven Estimates of Evapotranspiration and Its Controls in the Congo Basin. *Hydrol. Earth Syst. Sci.* **2020**, *24*, 4189–4211. [CrossRef]
27. Hersbach, H.; Bell, B.; Berrisford, P.; Biavati, G.; Horányi, A.; Muñoz Sabater, J.; Nicolas, J.; Peubey, C.; Radu, R.; Rozum, I.; et al. ERA5 monthly averaged data on single levels from 1940 to present. Copernicus Climate Change Service (C3S) Climate Data Store (CDS). 2023. Available online: https://cds.climate.copernicus.eu/datasets/reanalysis-era5-single-levels-monthly-means?tab=overview (accessed on 31 January 2025).
28. Muñoz Sabater, J. ERA5-Land Monthly Averaged Data from 1950 to Present. Copernicus Climate Change Service (C3S) Climate Data Store (CDS). 2019. Available online: https://cds.climate.copernicus.eu/datasets/reanalysis-era5-land-monthly-means?tab=overview (accessed on 31 January 2025).
29. Beaudoing, H.; Rodell, M. *GLDAS Noah Land Surface Model L4 monthly 0.25 × 0.25 Degree V2.1*; Goddard Earth Sciences Data and Information Services Center (GES DISC): Greenbelt, MD, USA, 2020. [CrossRef]
30. Global Modeling and Assimilation Office (GMAO). *MERRA-2 tavgU_2d_lnd_Nx: 2d, diurnal, Time-Averaged, Single-Level, Assimilation, Land Surface Diagnostics V5.12.4*; Goddard Earth Sciences Data and Information Services Center (GES DISC): Greenbelt, MD, USA, 2015. [CrossRef]
31. Abatzoglou, J.T.; Dobrowski, S.Z.; Parks, S.A.; Hegewisch, K.C. Data Descriptor: TerraClimate, a High-Resolution Global Dataset of Monthly Climate and Climatic Water Balance from 1958–2015. *Sci. Data* **2018**, *5*, 170191. [CrossRef]
32. Miralles, D.G.; Bonte, O.; Koppa, A.; Baez-Villanueva, O.M.; Tronquo, E.; Zhong, F.; Beck, H.E.; Hulsman, P.; Dorigo, W.; Verhoest, N.E.C.; et al. GLEAM4: Global Land Evaporation and Soil Moisture Dataset at 0.1° Resolution from 1980 to near Present. *Sci. Data* **2025**, *12*, 416. [CrossRef]
33. Zhang, K.; Chen, H.; Ma, N.; Shang, S.; Wang, Y.; Xu, Q.; Zhu, G. A Global Dataset of Terrestrial Evapotranspiration and Soil Moisture Dynamics from 1982 to 2020. *Sci. Data* **2024**, *11*, 445. [CrossRef]
34. Yu, G.-R.; Wen, X.-F.; Sun, X.-M.; Tanner, B.D.; Lee, X.; Chen, J.-Y. Overview of ChinaFLUX and Evaluation of Its Eddy Covariance Measurement. *Agric. For. Meteorol.* **2006**, *137*, 125–137. [CrossRef]
35. Yin, L.; Tao, F.; Chen, Y.; Liu, F.; Hu, J. Improving Terrestrial Evapotranspiration Estimation across China during 2000–2018 with Machine Learning Methods. *J. Hydrol.* **2021**, *600*, 126538. [CrossRef]
36. Pan, M.; Fisher, C.K.; Chaney, N.W.; Zhan, W.; Crow, W.T.; Aires, F.; Entekhabi, D.; Wood, E.F. Triple Collocation: Beyond Three Estimates and Separation of Structural/Non-Structural Errors. *Remote Sens. Environ.* **2015**, *171*, 299–310. [CrossRef]
37. Loew, A.; Schlenz, F. A Dynamic Approach for Evaluating Coarse Scale Satellite Soil Moisture Products. *Hydrol. Earth Syst. Sci.* **2011**, *15*, 75–90. [CrossRef]
38. Moran, P.A.P. Rank Correlation Methods, Royal Statistical Society. *J. Ser. A Gen.* **1951**, *114*, 99–100. [CrossRef]

39. Oliver, J.E. Monthly Precipitation Distribution: A Comparative Index. *Prof. Geogr.* **1980**, *32*, 300–309. [CrossRef]
40. Koppa, A.; Rains, D.; Hulsman, P.; Poyatos, R.; Miralles, D.G. A Deep Learning-Based Hybrid Model of Global Terrestrial Evaporation. *Nat. Commun.* **2022**, *13*, 1912. [CrossRef]
41. Zhong, F.; Jiang, S.; van Dijk, A.I.J.M.; Ren, L.; Schellekens, J.; Miralles, D.G. Revisiting Large-Scale Interception Patterns Constrained by a Synthesis of Global Experimental Data. *Hydrol. Earth Syst. Sci.* **2022**, *26*, 5647–5667. [CrossRef]
42. Hulsman, P.; Keune, J.; Koppa, A.; Schellekens, J.; Miralles, D.G. Incorporating Plant Access to Groundwater in Existing Global, Satellite-Based Evaporation Estimates. *Water Resour. Res.* **2023**, *59*, e2022WR033731. [CrossRef]
43. Liu, S.; Li, X.; Xu, Z.; Che, T.; Xiao, Q.; Ma, M.; Liu, Q.; Jin, R.; Guo, J.; Wang, L.; et al. The Heihe Integrated Observatory Network: A Basin-Scale Land Surface Processes Observatory in China. *Vadose Zone J.* **2018**, *17*, 1–21. [CrossRef]
44. Liu, S.M.; Xu, Z.W.; Che, T.; Li, X.; Xu, T.R.; Ren, Z.G.; Zhang, Y.; Tan, J.L.; Song, L.S.; Zhou, J.; et al. A Dataset of Energy, Water Vapor, and Carbon Exchange Observations in Oasis–Desert Areas from 2012 to 2021 in a Typical Endorheic Basin. *Earth Syst. Sci. Data* **2023**, *15*, 4959–4981. [CrossRef]
45. Zhou, L.; Geng, J.; Zhou, G.; Zhang, S.; Wu, Y. A Dataset of Carbon and Water Fluxes in the Winter Wheat and Summer Maize Rotation Ecosystem at Gucheng Station (2020–2022). *China Sci. Data* **2023**, *8*, 1–10. [CrossRef]
46. Zhang, S.; Zhou, L.; Zhou, G.; Jia, Q.; Li, R.; Wang, Y. A Dataset of Carbon and Water Flux Observations in the Agricultural Ecosystem of Spring Maize in Jinzhou (2005–2014). *China Sci. Data* **2023**, *8*, 1–12. [CrossRef]
47. Zhou, Y.; Zhang, Y.; Zhu, T.; Ju, W. A Dataset of Carbon and Water Fluxes in the Cropland Ecosystem at Jurong Station (2015–2020). *China Sci. Data* **2023**, *8*, 1–11. [CrossRef]
48. Liu, F.; Shen, Y.; Cao, J.; Zhang, Y. A Dataset of Water, Heat, and Carbon Fluxes over the Winter Wheat-Summer Maize Croplands in Luancheng during 2013–2017. *China Sci. Data* **2023**, *8*, 1–10. [CrossRef]
49. Jia, Q.; Wen, R.; Zhou, L.; Zhou, G.; Xie, Y.; Wu, Q. A Dataset of the Observations of Carbon and Water Fluxes in the Paddy Fields of Panjin (2018–2020). *China Sci. Data* **2023**, *8*, 1–12. [CrossRef]
50. Zhao, F.; Li, F.; Zhan, C.; Zhang, L.; Chen, Z. A Carbon and Water Fluxes Dataset of the Farmland Ecosystem of Winter Wheat and Summer Maize in Yucheng (2003–2010). *China Sci. Data* **2021**, *6*, 1–7. [CrossRef]
51. Dong, G.; Wang, Y.; Wang, K.; Jiang, S.; Shao, C. A Dataset of Carbon and Water Fluxes in the Changling Alkali-Saline Paddy Rice Fields in the Songnen Plain, China (2018–2020). *China Sci. Data* **2023**, *8*, 1–15. [CrossRef]
52. Qi, D.; Fei, X.; Song, Q.; Zhang, Y.; Sha, L.; Liu, Y.; Zhou, W.; Lu, Z.; Fan, Z. A Dataset of Carbon and Water Fluxes Observation in Subtropical Evergreen Broad-Leaved Forest in Ailao Shan from 2009 to 2013. *China Sci. Data* **2021**, *6*, 1–11. [CrossRef]
53. Niu, X.; Sun, P.; Tao, S.; Chen, Z.; Niu, B.; Liu, S. A Dataset of Carbon and Water Fluxes in a Natural Oak Forest of Baotianman in Henan Province (2017–2018). *China Sci. Data* **2023**, *8*, 1–10. [CrossRef]
54. Yang, S.; Liu, J.; Yang, C.; Lan, G.; Song, B.; Wu, Z. A Dataset of Carbon and Water Fluxes and Micrometerological Elements in Danzhou Rubber Plantation (2010–2018). *China Sci. Data* **2022**, *7*, 1–13. [CrossRef]
55. Li, Y.; Yan, J.; Meng, Z.; Huang, J.; Zhang, L.; Chen, Z.; Liu, S.; Chu, G.; Zhang, Q.; Zhang, D. An Observation Dataset of Carbon and Water Fluxes in a Mixed Coniferous Broad-Leaved Forest at Dinghushan, Southern China (2003–2010). *China Sci. Data* **2021**, *6*, 1–11. [CrossRef]
56. Yan, Y.; Zhou, L.; Zhou, G.; Jia, B.; Song, J.; Zhang, S. A Dataset of Carbon and Water Fluxes of the Boreal Forest Ecosystem in Huzhong (2014–2018). *China Sci. Data* **2023**, *8*, 1–10. [CrossRef]
57. Tang, X.; Kong, D.; Chen, Y.; Li, Y.; Qian, F.; Ding, Z.; Ma, M. A Dataset of Carbon and Water Fluxes Observations in Subtropical Evergreen Broad-Leaved Forest in Jinfo Mountain from 2020 to 2021. *CSDATA* **2023**, *8*, 1–9. [CrossRef]
58. Wang, Y.; Luo, W.; Chen, J.; Cai, X.; Zhang, L.; Cheng, A.; Wang, S. A Dataset of Carbon and Water Fluxes in the Sample Plots of Natural Regeneration at Puding Station of Guizhou Province (2015–2019). *China Sci. Data* **2023**, *8*, 1–9. [CrossRef]
59. Dai, X.; Wang, H.; Xu, M.; Yang, F.; Wen, X.; Chen, Z.; Zhang, L.; Sun, X.; Yu, G. An Observation Dataset of Carbon and Water Fluxes of Artificial Coniferous Forests in Qianyanzhou (2003–2010). *China Sci. Data* **2021**, *6*, 1–9. [CrossRef]
60. Qi, D.; Zhang, Y.; Song, Q.; Fei, X.; Sha, L.; Liu, Y.; Zhou, W.; Zhou, L.; Deng, X.; Luo, Y.; et al. A Dataset of Carbon, Water and Energy Fluxes Observed in Xishuangbanna Tropical Seasonal Rain Forest from 2003 to 2010. *China Sci. Data* **2021**, *6*, 1–13. [CrossRef]
61. Liu, Y.; Zhang, J.; Zheng, H.; Fei, X.; Sha, L.; Zhou, W.; Zhou, L.; Deng, X.; Luo, Y.; Deng, Y.; et al. A Dataset of Carbon and Water Fluxes Observed in Xishuangbanna Tropical Seasonal Rain Forest from 2011 to 2015. *China Sci. Data* **2023**, *8*, 1–13. [CrossRef]
62. Yu, H.; Qi, D.; Zhang, Y.; Sha, L.; Liu, Y.; Zhou, W.; Deng, Y.; Song, Q. An Observation Dataset of Carbon and Water Fluxes in Xishuangbanna Rubber Plantations from 2010 to 2014. *China Sci. Data* **2021**, *6*, 1–12. [CrossRef]
63. Huang, H.; Zhou, Y.; Zhang, J.; Gao, X.; Liu, L.; Meng, P. A Dataset of Carbon and Water Flux Observations in a Quercus Variabilis Plantation in Xiaolangdi (2016–2017). *China Sci. Data* **2023**, *8*, 1–9. [CrossRef]
64. Du, J.; Luo, W.; An, Z.; Zhang, L.; Huang, H.; Hao, Y.; Wang, Y. A Dataset of Carbon and Water Fluxes over Typical Ecosystems in Beijing Yanshan Hilly Regions (2020–2021). *China Sci. Data* **2023**, *8*, 1–9. [CrossRef]

65. Wu, J.; Guan, D.; Wang, A.; Yuan, F.; Diao, H.; Yu, G.; Chen, Z.; Zhang, L. A Dataset of Carbon and Water Flux Observation in a Broad-Leaved Red Pine Forest in Changbai Mountain (2003–2010). *China Sci. Data* **2021**, *6*, 1–10. [CrossRef]
66. Che, T.; Li, X.; Liu, S.; Li, H.; Xu, Z.; Tan, J.; Zhang, Y.; Ren, Z.; Xiao, L.; Deng, J.; et al. Integrated Hydrometeorological, Snow and Frozen-Ground Observations in the Alpine Region of the Heihe River Basin, China. *Earth Syst. Sci. Data* **2019**, *11*, 1483–1499. [CrossRef]
67. Song, J.; Zhou, L.; Zhou, G.; Yan, Y.; Zhang, S. A Dataset of Carbon and Water Fluxes of the Temperate Desert Steppe in Damao Banner, Inner Mongolia (2015–2018). *China Sci. Data* **2023**, *8*, 1–9. [CrossRef]
68. Chai, X.; He, Y.; Shi, P.; Zhang, X.; Niu, B.; Zhang, L.; Chen, Z. An Observation Dataset of Carbon and Water Fluxes over Alpine Meadow in Damxung (2004–2010). *China Sci. Data* **2021**, *6*, 1–10. [CrossRef]
69. Zhang, F.; Si, M.; Guo, X.; Cao, G.; Zhang, Z. A Dataset of the Observations of Carbon, Water and Heat Fluxes over an Alpine Meadow in Haibei (2015–2020). *China Sci. Data* **2023**, *8*, 1–10. [CrossRef]
70. You, C.; Wang, Y.; Chen, S. A Dataset of Carbon and Water Fluxes of the Typical Grasslands in Duolun County, Inner Mongolia during 2006–2015. *China Sci. Data* **2023**, *8*, 1–11. [CrossRef]
71. Hao, Y.; Zhang, L.; Sun, X.; Yu, G.; Chen, Z.; Wang, Y. A Dataset of Carbon and Water Fluxes over Xilinhot Temperate Steppe in Inner Mongolia (2003–2010). *China Sci. Data* **2021**, *6*, 1–7. [CrossRef]
72. Wang, Y.; You, C.; Chen, S. A Dataset of Carbon and Water Fluxes of Mowing Grasslands in Xilinhot, Inner Mongolia during 2006–2015. *China Sci. Data* **2023**, *8*, 1–10. [CrossRef]
73. Chen, W.; Wang, S.; Niu, S. A Dataset of Carbon, Water and Heat Fluxes of Zoige Alpine Meadow from 2015 to 2020. *China Sci. Data* **2023**, *8*, 1–8. [CrossRef]
74. He, F.; Li, Q.; Chen, D.; Zhao, L. A Dataset of Carbon, Water and Heat Fluxes over an Elymus Nutans Artificial Grassland in the Sanjiangyuan Area (2012–2016). *China Sci. Data* **2023**, *8*, 1–10. [CrossRef]
75. Qi, D.; Yang, D.; Song, Q.; Liu, Y.; Zhang, Y.; Fei, X.; Sha, L.; Zhou, W.; Chen, A.; Wen, G.; et al. An Observation Dataset of Carbon and Water Fluxes at Yuanjiang Dry-Hot Valley Ecological Station (2013–2015). *China Sci. Data* **2021**, *6*, 1–13. [CrossRef]
76. Zhang, F.-W.; Li, H.; Zhao, L.; Zhang, L.; Chen, Z.; Zhu, J.; Xu, S.; Yang, Y.; Zhao, X.; Yu, G.; et al. An Observation Dataset of Carbon, Water and Heat Fluxes of Alpine Shrubland in Haibei (2003–2010). *China Sci. Data* **2021**, *6*, 1–10. [CrossRef]
77. Zhang, F.; Li, H.; Zhang, L.; Li, J.; Yang, Y.; Yu, G.; Li, Y. A Dataset of the Observations of Carbon, Water and Heat Fluxes over an Alpine Shrubland in Haibei (2011–2020). *China Sci. Data* **2023**, *8*, 1–11. [CrossRef]
78. Han, C.; Mu, Y.; Zha, T.; Qin, S.; Liu, P.; Tian, Y.; Jia, X. A Dataset of Ecosystem Fluxes in a Shrubland Ecosystem of Mau Us Sandy Land in Yanchi, Ningxia, China (2012–2016). *Chin. J. Plant Ecol.* **2023**, *47*, 1322–1332. [CrossRef]
79. Zhang, M.; Xiao, W.; Zhao, J.; Jia, L.; Ge, P.; Bao, H.; Qiu, J.; Zhang, Z.; Zhao, R.; Wang, J.; et al. A Dataset of Carbon and Water Flux Observed in Aquaculture Ponds in Quanjiao, Anhui Province from 2016 to 2020. *China Sci. Data* **2023**, *8*, 1–17. [CrossRef]
80. Zhang, F.; Li, H.; Zhao, L.; Zhang, L.; Chen, Z.; Zhu, J.; Xu, S.; Yang, Y.; Zhao, X.; Yu, G.; et al. An Observation Dataset of Carbon, Water and Heat Fluxes in an Alpine Wetland in Haibei (2004–2009). *China Sci. Data* **2021**, *6*, 1–10. [CrossRef]
81. Wei, S.; Li, P.; Chu, X.; Song, W.; Wang, X.; Zhao, M.; Zhang, X.; Han, G. A Dataset of Carbon and Water Fluxes in a Phragmites Australis Wetland in the Yellow River Delta during 2011–2018. *China Sci. Data* **2024**, *9*, 1–10. [CrossRef]

Disclaimer/Publisher's Note: The statements, opinions and data contained in all publications are solely those of the individual author(s) and contributor(s) and not of MDPI and/or the editor(s). MDPI and/or the editor(s) disclaim responsibility for any injury to people or property resulting from any ideas, methods, instructions or products referred to in the content.